Nanoscopy through a plasmonic nano-lens

Matthew J Horton[1], Oluwafemi S Ojambati[1], Rohit Chikkaraddy[1], William M Deacon[1], Nuttawut Kongsuwan[2], Angela Demetriadou[2,3], Ortwin Hess[2], Jeremy J Baumberg[1]

[1] NanoPhotonics Centre, Cavendish Laboratory, Department of Physics, JJ Thompson Avenue, University of Cambridge, Cambridge, CB3 0HE, UK
[2] Blackett Laboratory, Imperial College London, South Kensington Campus, London, SW7 2AZ, UK
[3] School of Physics and Astronomy, University of Birmingham, Birmingham, B15 2TT, UK

Significance statement
Imaging of single to few molecules has received much recent interest. While super-resolution microscopies access sub-diffraction resolution, they do not work for plasmonic hotspots due to the loss of positional information that results from plasmonic coupling. Here, we show how to reconstruct the spatial locations of molecules within a plasmonic hot spot with 1 nm precision. We use a plasmonic nano-ball-lens to demonstrate for the first time that plasmonic nanocavities can be used simultaneously as a nanoscopic and spectroscopic tool. This work opens up new possibilities for studying the behaviour of few to single molecules in plasmonic nanoresonators, while simultaneously tracking their movements and spectral features. Our plasmonic nano-lens is useful for nanosensing, nanochemistry, and biofunctional imaging.

Abstract
Plasmonics now delivers sensors capable of detecting single-molecules. The emission enhancements and nanometre-scale optical confinement achieved by these metallic nanostructures vastly increase spectroscopic sensitivity, enabling real-time tracking. However, the interaction of light with such nanostructures typically loses all information about the spatial location of molecules within a plasmonic hot spot. Here we show that ultrathin plasmonic nanogaps support complete mode sets which strongly influence the far-field emission patterns of embedded emitters, and allow the reconstruction of dipole positions with 1 nm precision. Emitters in different locations radiate spots, rings and askew halo images, arising from interference of two radiating antenna modes differently coupling light out of the nanogap, highlighting the imaging potential of these plasmonic 'crystal balls'. Emitters at the centre are now found to live indefinitely, because they radiate so rapidly.

Introduction

Confining and coupling light to nanoscale objects is at the heart of nanophotonics (1). The possibility of imaging, localizing, and eventually manipulating nano-objects down to the level of single emitters is highly desirable for many applications and fundamental studies (2, 3). Approaches include the development of super-resolution microscopies such as STED, SIM, STORM and PALM, (4, 5) however there has also been intense interest in plasmonic nanostructures that utilize collective charge oscillations in noble metals to enhance the optical fields within a few nanometres (6). This extreme confinement of optical fields has significant implications for nanoscale sensing (7), advanced spectroscopies (8), biological applications (9), single atom optics (10), and quantum (11, 12) and nonlinear photonics (13).

The tightly-confined fields in plasmonic nanocavities enhance the fluorescence intensity of dye molecules and their high optical density of states reduces the molecule's emission lifetime (14–17). However, this enhanced emission comes at the cost of misrepresenting the position of individual molecules near the

metallic structure. (18–20) Emitters in the vicinity of a nanoparticle radiate into the far-field via the plasmon mode and therefore appear displaced either towards or away from the nanoparticle centre, by up to 100 nm. (21) Similarly, the interaction of dye molecules with colloidal aggregates can produce surface-enhanced Raman scattering (SERS) signals spatially shifted from the nanoparticle photo-luminescence. (22) While super-resolution microscopies access sub-diffraction resolution, these techniques are currently impractical for plasmonic nanocavities due to this loss of positional information associated with plasmonic out-coupling. (23) Circumventing this limitation would allow plasmonic nanocavities to be simultaneously used as a nanoscopic and nano-spectroscopic tool.

Here we show how careful selection of the plasmonic architecture controls the confined optical modes, so that measurements of the far-field radiation patterns access near-field positional information. To generate high-quality high-volume data, we explore the nanoparticle-on-mirror (NPoM) architecture which consists of a Au nanoparticle coupled to its image charges on a Au mirror from which it is separated by a self-assembled molecular layer (24, 25). This architecture forms extremely robust reliable plasmonic nanocavities, is easily produced using self-assembly, and allows for the study of thousands of identical structures on a single substrate. In this study, near-spherical gold nanoparticles (NPs) with diameters D=60 or 80 nm are placed on flat gold mirrors after uniformly coating them with molecules of methylene blue (MB), each individually encapsulated inside a molecular container of cucurbit[7]uril (CB[7]). The CB[7] binds strongly to Au, with its molecular height ensuring a constant spacing of d=0.9 nm between the gold nanoparticle and the gold mirror beneath (25–27), while also protecting the dye molecules and orienting them vertically.

Results

Theory and simulations

Previous studies utilizing NPoMs (also known as particle-over-substrate, metal-insulator-metal waveguide, nanogap patch antenna (6) and equivalent to nanoparticle dimers, dumbbells (28) or homodimers (29)) suggest that light in the cavity is out-coupled through one of two antenna modes, either a transverse particle mode or a longer-wavelength vertical-field gap mode (6, 30–32). Recent works show that emitters in the NPoM gap radiate dominantly through the gap mode, because of its stronger enhancement and radiative efficiency (33, 34). Because the optical field in the gap is mostly z-polarized (oriented as in Fig.1), one would expect out-coupled light from these emitters to emerge at high angles from the dimer axis and thus produce ring-shaped distributions in the far-field after collection through high-NA microscope objectives.

Here we show this is not the case, and that emission from molecules within nanoscale plasmonic gaps depends on non-negligible contributions from a large number of nanocavity modes. Furthermore, the coupling to each of these modes is highly dependent on the precise position of the molecules in the gap, which can therefore be inferred from the far-field spatial distribution of the out-coupled light. We first explore this complexity by solving Maxwell's equations using finite element methods (FEM, see Methods and (35)). We obtain the far-field emission image of a dipole emitting at $\lambda = 660$ nm inside an 80 nm NPoM with gap d=1 nm and facet diameter w=20 nm, as it is shifted along the x direction by up to 15 nm (Fig.1). Our calculations show that the far-field ring emission seen for an on-axis dipole changes and becomes askew within 1 nm lateral shift. Intriguingly, this nano-beaming tilts the far-field emission in the

opposite direction to the emitter displacement under the facet (Fig.1a,b). The same emission patterns are confirmed with finite-difference time-domain simulations (see supplementary Fig.S1).
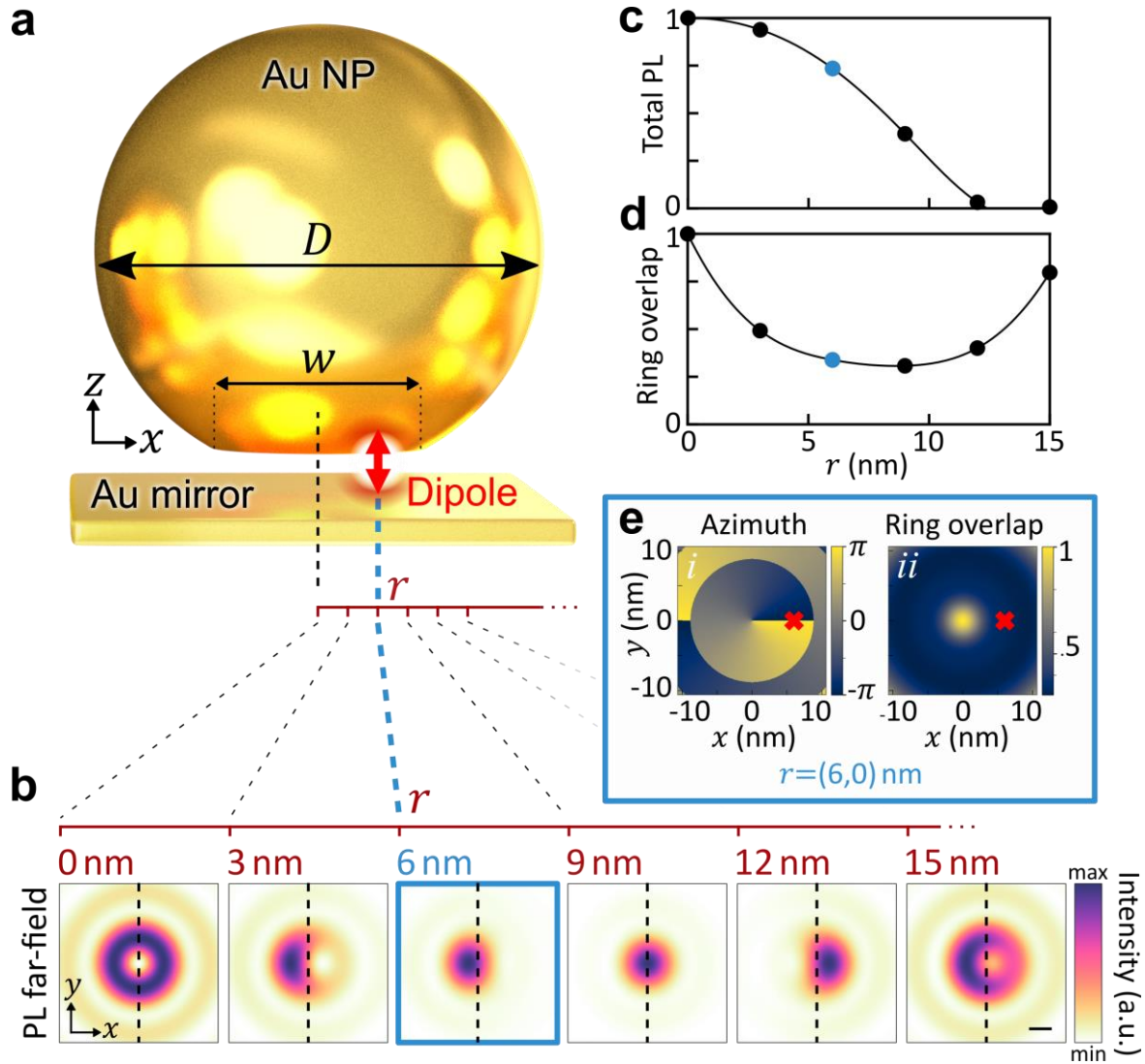

Fig.1 | Simulated far-field images from single emitter in the gap progressively shifted sideways. a, Schematic plasmonic nanoparticle-on-mirror (NPoM) with vertically oriented dipole emitter placed at r up to 15 nm offset from centre. **b,** Simulated far-field real-space images (normalized, λ=660 nm) after collection through high-NA objective (see text, camera image scale bar 100 μm). **c,** Emission intensity and **d,** ring overlap *vs* radial location of emitter. **e,** Extracted (*i*) azimuthal weight (ϕ_c) and (*ii*) ring-overlap integral (O_r) which reconstruct dipole position r. Red crosses give result for emitter shifted to x=6 nm.

To invert these near-field transforms, the centre of mass of each of the simulated images (x_c, y_c) is used to map the azimuthal orientation, $\phi_c = \text{atan}(y_c/x_c) + \xi_c$ (Fig.1e*i*). The overlap integral O_r with the ideal ring distribution (Fig.1b, r=0) is used to quantitatively derive the fraction of ring-like emission in images at each emitter position (Fig.1e*ii*,d). These then allow a one-to-one mapping from (ϕ_c, O_r) extracted from measured images, to the position of a single dipole, seen as red crosses in Fig.1e reconstructing r=(6, 0) nm dipole position (for details on this method, including definitions of ϕ_c and O_r, see

supplementary Fig.S2). We note that the total emission from the dipole (shown normalised in Fig.1b) falls strongly when it is >9 nm from the central location (Fig.1c), meaning $r>10$ nm is not observed.

To understand the peculiar behaviour of these emission images, we characterise the quasi-normal gap modes (found using QNMEig (36)) and their out-coupling efficiencies using a near- to far-field conversion (37). The resulting angular emission when passed through appropriate Fourier filtering (see supplementary methods) gives images matching those shown in Fig.1b. As well known for spherical NPoMs or dimers, the (10) gap mode dominates at low energies, however as the gap facet widens (Fig.2a) the energies of higher order modes drop and either cross (20) or anticross (11) this mode (34) [for (lm) nomenclature see supplementary note]. All other modes (grey) are dark and, while the symmetric $(l0)$ modes dominate emission (Fig.2b), the $(l1)$ modes emit through in-plane antenna dipoles (as seen in the angular emission pattern Fig.2f) which are ten-fold weaker but not negligible. We emphasise that since for such small gaps the gap fields are z polarized, only the z-oriented dipole components contribute to emission.
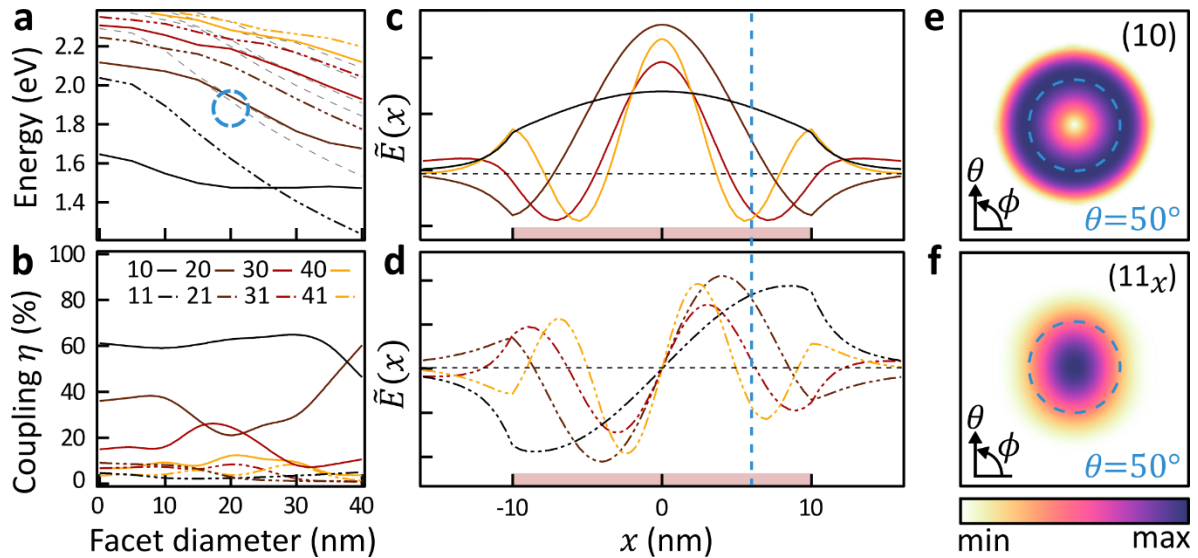

Fig.2 | Plasmonic nanogap cavity modes of 80 nm NPoM with 1 nm gap and 20 nm facet diameter. a, Mode energies and b, outcoupling efficiencies for the first 4 symmetric [solid lines (lm)=(10)-(40)] and asymmetric [dashed (11)-(41)] nanogap modes. Blue circle marks regime for facets of a typical $D{\sim}80$ nm NPoM. c,d, Corresponding near-field mode amplitudes with a 20 nm facet (normalised, colours as in a, dashed vertical at x=6 nm, extent of facet indicated by a pale red bar on the x-axis). e,f, far-field angular emission patterns up to 50° collection aperture for (10) and (11_x) emission.

For the 80 nm NPoMs used here with MB dyes (660 nm, 1.88 eV), facet sizes of 20 nm are typical (38) leading to operation in the regime marked by the dashed circle. These emit typically into a combination of {10,20,11} modes, depending not only on the spectral overlaps, but also on the spatial overlaps of the near-field modes with the emitter location (Fig.2c,d). For example for an emitter at x=6 nm (blue vertical dashed), the relative phase and amplitude of x-polarised (11_x) and radially-polarised (10,20) antenna emission combine to give the displaced spot (in the opposite direction as seen in Fig.1b) shifted by several times the λ/NA resolution. The reversed spot displacement for x>9 nm (Fig.1b) can then be understood to arise from the change in sign of the (20,21) modes near the facet edge (Fig.2c,d). These crossovers do not vary substantially with the experimental range of facet sizes (supplementary Fig.S3). Placing a

plasmonic Au sphere on top of an emitter thus acts as a nanolens or plasmonic refracting globe, capable of expanding the resolvable field of view into the nano regime.

Experimental

To observe this nanolens effect, we alternately record dark-field scattering and light emission from the same NPoM over time. To efficiently excite the gap mode, we use a radially-polarized continuous wave laser with a wavelength of 633 nm and power density of 150 $\mu W.\mu m^{-2}$ at the focus. Samples created across large areas ($4 \times 4\,mm^2$, see Methods) show consistent dark-field scattering spectra with the lowest (10) mode centred at $\lambda_{10} \sim 730$ nm (see below and supplementary Fig.S4-5), close to the MB dye emission at 690 nm. Hundreds of nanoparticles are individually imaged and spectroscopically analysed (24, 25), with the emitted light spatially magnified (~3500 times) onto the entrance slit of a monochromator after spectrally filtering out the 633 nm excitation laser (Fig.3). The dark-field image from white-light scattering off each NPoM is <u>always</u> a ring (Fig.3a, Fig.5a-d, supplementary Fig.S4), because z-polarised gap modes dominate the in/out coupling (Fig.2b) converting the multimode excitation into a single spatial mode upon re-radiation. Slight asymmetries in the dark-field images are mostly due to the polarisation sensitivity of our optical system, leading to slightly greater intensity along the vertical axis relative to the horizontal axis. Inelastic light emission, on the other hand, is a combination of photoluminescence (PL), surface-enhanced resonant Raman scattering (SERRS), and background electronic Raman scattering (ERS) from the Au, and gives very different spatial shapes. Indeed sometime rings are observed (Fig.3b), but also partial rings (termed 'askew', presenting a partial halo surrounding an off-centre dark central spot) as well as bright 'spots' which have no dark centre. For each category, the inelastic emission shows similar emission spectra (Fig.3d) implying that they all originate from the same dye molecules. Samples with identical CB[7] spacers but without dyes show negligible emission but identical dark field spectra (supplementary Fig.S6), confirming the dye emitters indeed form local light sources.
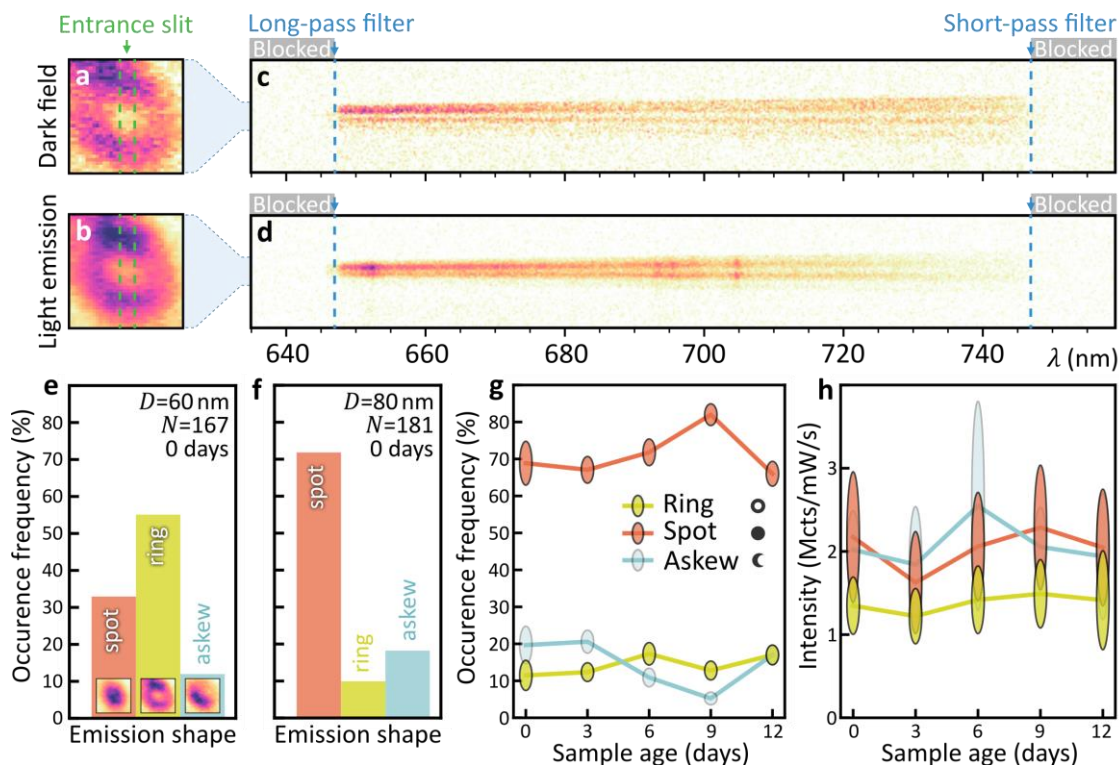
Fig.3 | Real-space scattering and emission images from single NPoMs. a,b, Spectrally-integrated (647-747 nm) images of white-light dark-field scattering and light emission (in 'ring' state). **c,d,** Spectrally-resolved emission through a vertical cross section formed by the entrance slit (dashed in a,b) showing ring profile for both broadband photoluminescence and sharp SERS lines. **e-g,** Relative occurrence of each shape (insets in e) for (e) D=60 nm and (f,g) 80 nm nanoparticles. **h,** Integrated emission intensity of 80 nm NPs, as sample ages after initial preparation. Vertical ellipses give standard errors of (g) fractions and (h) intensities from $N(t)$ nanoparticles.

Categorizing >3000 identically prepared particles reveals that each category of far-field shape occurs with a consistent probability. While immediately after sample preparation (0 days) the larger 80 nm NPoMs show mostly spots with only 25% circular or askew rings (Fig.3f), this observation is reversed for 60 nm NPoMs which give >65% rings (Fig.3e). This extreme sensitivity to NP size suggests the strong influence of interacting gap modes, discussed further below. While nanoscale faceting (which changes with aging (39)) could influence emissive nano-lensing, we observe little change in these statistics for >10 days (Fig.3g,h) including little decrease in emission intensity (each time probing slightly different regions of the sample). This suggests that in the dark, both plasmonic and dye components of the construct are stable. These results should be compared to antenna-directed angular emission from dyes in the vicinity of other nanostructures. For example, high directivity of emission from Atto740-doped PMMA near gold nanorods has been observed (40), with emission patterns showing sensitivity to dye position on the order of 100 nm. Emission from Cy5.5 dye molecules near gold nanoislands shows similar sensitivity (21), as does the emission of quantum dots coupled to nanoscale Yagi-Uda structures (41).

Prolonged observation on a single NPoM, however reveals that the far-field emission intensity and distribution of a particle is not fixed, but instead varies with time under illumination (Fig.4a,b). For example, a nanoparticle which initially emits into a spot can gradually change to produce a ring-shaped emission (Fig.4b), or vice-versa (supplementary Fig.S8-10). Many particles are observed to wander between all three different scattering distribution types, at times returning to a previously observed type more than once (Fig.4a,b, supplementary Fig.S8). This evolution is accompanied by a gradual reduction in the overall emission intensity although the intensity tends to a steady value that is ~30 times higher than the background from a cavity without dyes, even after two hours irradiation (see supplementary Fig.S6-7). This implies that full bleaching is never observed, although full recovery of emission to initial levels is also never observed. This was confirmed in a second experiment by irradiating a single particle for four cycles each comprising 15 minutes illumination and 5 minutes rest in the dark, with little to no recovery in emission observed following each rest period.
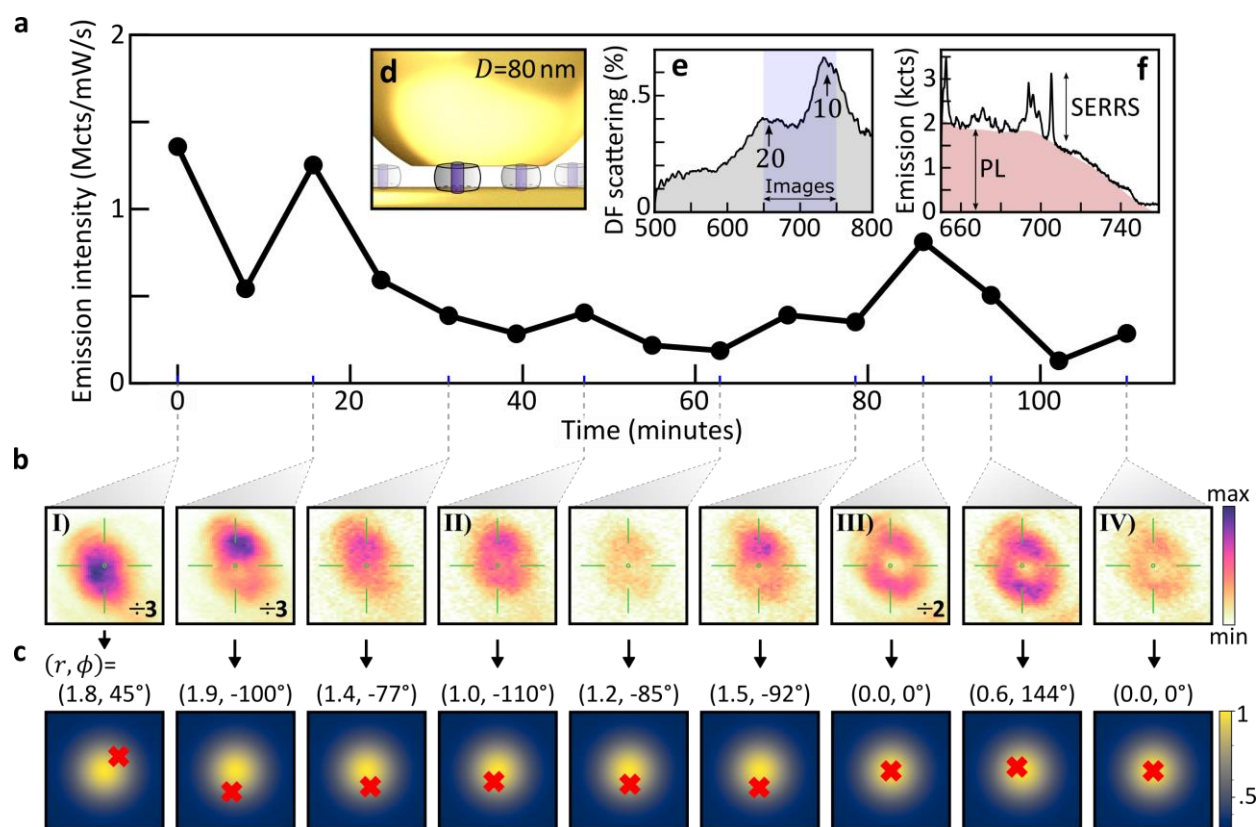
Fig.4 | Time evolution of real-space emission from a single 80 nm NPoM. a, Integrated intensity and **b,** corresponding real-space spectrally-filtered emission images at times marked, green reticle at dark-field ring centre. **c,** Ring-overlap integral map from COMSOL simulations (for $|x|,|y|<5$ nm), with reconstructed coordinates (r[nm],ϕ[°]) of weighted emitter position in NPoM cavity marked with red cross (see text). Note gradual movement toward centre of the facet over time (see text for discussion). **d,** Schematic MB dyes (blue) in CB within plasmonic gap. **e,** Dark-field elastic scattering spectrum, emission detection range shaded. **f,** Emission spectrum showing integrated emission is dominated by dye PL.

These changes in the emission intensity and far-field profile of individual plasmonic nanocavities suggest that emitters at different positions within the gap out-couple through different cavity modes at different times (Fig.4e, see Discussion). Since CB[7] forms monolayers with 0.24 molecules.nm^{-2}, (42) a 1:1 molar ratio of CB[7] to MB gives ~75 emitters within these gaps (for 80 nm NPoMs with 20 nm facets). Given the assembly protocol, these are expected to be randomly distributed across the nanogap (Fig.4d), although only ~19 contribute strongly to the (10) mode emission. We note that while complex changes to the SERRS spectra sometimes appear over time (supplementary Fig.S11) with changing Raman peak positions and intensities, we stress that the integrated emission is dominated (>85%) by the photoluminescence (Fig.4f).

Since the nanoparticle diameter sets the facet width which controls the spectral tuning of the NPoM gap modes, (38) the prevalence of rings (for D=60 nm) vs spots (for D=80 nm) suggests the crucial importance of precisely which range of gap modes into which the molecules emit (Fig.3e,f). Exploring more carefully the differences between 80 nm NPoMs which originally show rings vs spots (Fig.5, supplementary Fig.S4) provides further evidence. While NPoMs with spot-shaped emission generally give dark-field scattering spectra dominated by the (10) resonance (Fig.5c,d), the NPoMs with ring-shaped emission show also the

higher-energy (20) resonance around 640 nm (Fig.5a,b). This is confirmed by extracting the resonance peak positions from the scattering spectra of 1602 NPoMs showing this trend is robust (Fig.5e). Similar scattering spectral changes accompany the evolution of shape during time-resolved experiments (Fig.4, and supplementary Fig.S8-10). The (20) mode increases out-coupling at shorter wavelengths, thus broadening the spectral emission from ring-NPoMs compared to spot-NPoMs. Askew NPoMs have similar emission spectra (not shown) to the spot-NPoMs.
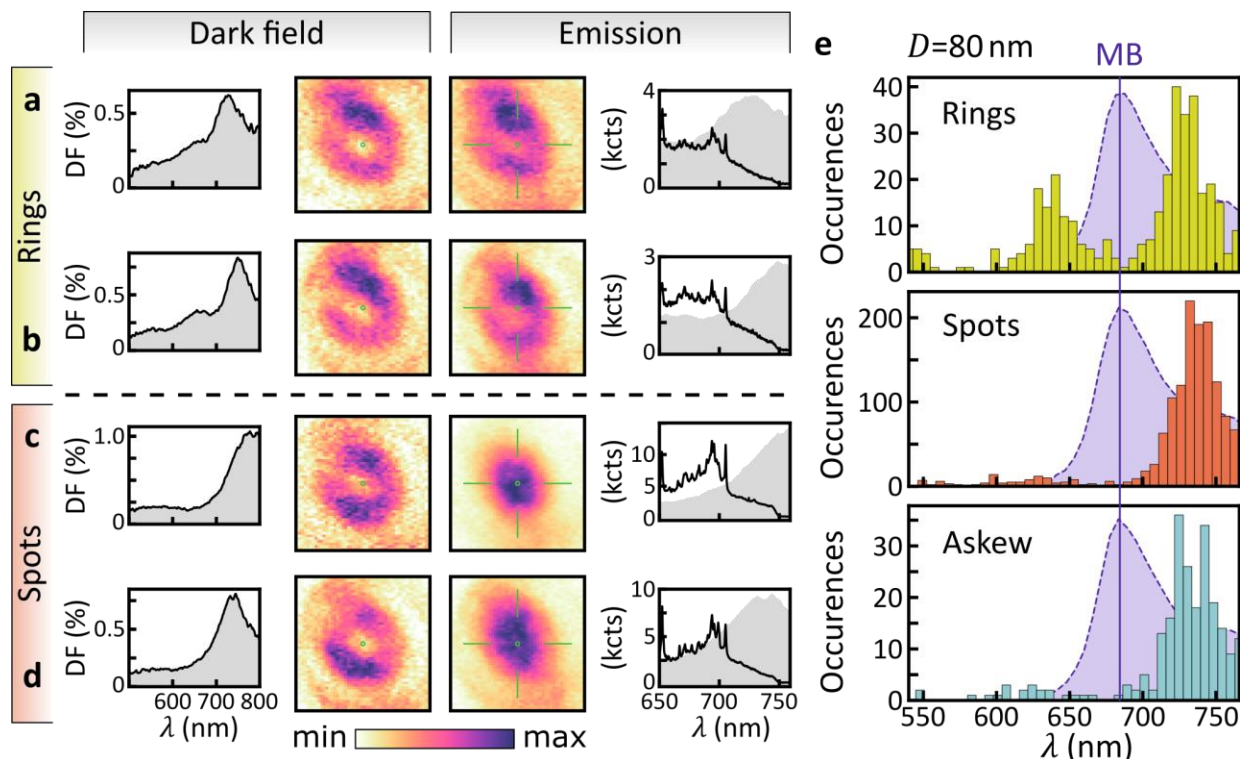
Fig.5 | Comparison of ring and spot emission from 80 nm NPoMs. a-d, from left to right: dark field spectra, dark field image, emission image, and emission spectra, for NPoMs exhibiting (a,b) rings and (c,d) spots. e, Analysis of scattering spectra peak central wavelengths classed by shape, for 1602 NPoMs. Shaded grey curves in emission spectra (a-d) are same dark field spectra. Purple shaded curves in e show the MB dye emission in solution.

Discussion

Emission into a ring implies that dyes near the central axis of the NP must dominate (see Fig.1 and supplementary Fig.S3, Fig.S12). Experiments show these rings emerge with most 60 nm NPoMs ($\lambda_{10} \sim 680$ nm) and for those 80 nm NPoMs ($\lambda_{10} \sim 730$ nm) with a larger facet ($w > 25$ nm, estimated from the (20) resonance position). With smaller facets and smaller NPs, the (10) mode is more tightly confined (nearly 3-fold closer to the axis when w reduces from 20 nm to 0 nm) so that only dyes within 2 nm of the facet centre experience strong Purcell factor enhancements and high quantum yield of emission (43) (see Fig.1). This explains the 60 nm NPoM data since the smaller size and facets of these NPs imply emission from ~3 centrally-positioned MB dyes, where the MB emission is tuned resonantly to the lowest gap plasmon. For comparison, only dyes within 3 nm of the facet centre produce rings in 80 nm NPoMs, which at a surface packing density of 0.24 molecules.nm^{-2},(42) implies emission from <7 molecules. After bleaching (such as observed in Fig.4), this reduces to ≤3 molecules.

The bright spots seen initially from the 80 nm NPoMs (as in Fig.5c,d) must arise from multiple dyes at different positions ranging across the facet. In this situation the coordinates given in Fig.4c must be interpreted as the average position of emitters, indicating the location of the greatest dye concentration. For a w=20 nm facet, the most likely dye location for outcoupling the PL is at r=4.5 nm for the (10) mode, which will give a spot in the far-field (see supplementary Fig.S13). This increases to r=9.1 nm for the (11) mode which is spectrally resonant with the PL, although it out-couples 25 times more weakly (Fig.2b). Either coherently or incoherently summing the emission from multiple dyes randomly placed under the NPoM indeed predicts spot-like emission (supplementary Fig.S12).

The full interplay of facet size and emitter position is complex in producing different emission shapes. However askew ring-like distributions always indicate an off-centre emitter, with the degree of asymmetry dependent on the emitter's radial coordinate and thus allowing the nanoscale position of the dye to be estimated. When the facet size is known, along with the maximum emission intensity per dye (when placed at the nanocavity centre), a full inversion of the patterns can yield the relative position of each dye. This is possible due to the fundamental symmetries of the (10), (20), and (11) modes in the near- and far-field, which is a feature of not only facetted spherical NPoMs, but also for example, nanocubes-on-mirror (34). A small change in gap size does not change our inversion technique, and only slightly updates the appropriate mapping (see supplementary note, and supplementary Fig.S17Fig.S18). Similarly different nanoparticle shapes lead to modified mappings from those shown in Fig.1e and supplementary Fig.S2.

However because the emitters can be strongly coupled by the plasmonic gap modes (25, 44, 45), emitters can be coherently coupled together, and jointly emit into the plasmonic gap modes which subsequently radiate, further complicating the picture outlined here. To avoid this, the samples used here are in the weak coupling regime since there is a large detuning between the dye emission peak and the cavity resonance of the 60 nm and 80 nm NPoMs compared to the 40 nm NPoMs used in (25). The smaller 40 nm NPs have a smaller scattering strength ($\propto D^6$) and have fewer molecules in the nanogap due to their smaller facet size ($w\sim$6 nm), making the emission too weak to resolve spatially. Measurements on strongly-coupled systems would however be extremely interesting for the observation of spatial coherent interactions between the emitters and nanocavity.

The MB dye is chosen for our experiments not only because it is tuned into the weak coupling regime, but because it is the longest-wavelength dye that fits within a CB[7]. Any further detuning of the dye emission peak from the cavity resonance makes emission too weak to resolve spatially. However, since simulations show that a different emission wavelength simply leads to the spot/ring transitions occurring at different emitter positions to those observed with a 660 nm wavelength, tuning the emission wavelength is completely analogous to changing the NPoM size, which is more easily studied experimentally.

The progression from spots to rings seen in time (Fig.4 and supplementary Fig.S8-10) can be understood from the progressive bleaching of different dyes, and rules out the possibility of different emission patterns being due to nm-scale surface roughness features on the Au mirror (32). However, it also points to a surprising feature, since the convergence to rings at longer times implies that the dyes which last longest are always at the centre of the facets. This suggests that either the narrow gaps physically protect molecules on the inside from photochemical attack, and/or that the Purcell factors for the dyes at the centre (F_P>3000, (43)) are so high that the molecules emit their photons before any chemical attack or

intersystem crossing is possible. While encapsulation of dyes in CB[7] is known to partially protect them from bleaching (46, 47), this is unable to explain the extreme stability observed here.

One possible explanation for the sporadic transient revivals of emission could be lateral diffusion of dyes in and out of the hotspots. However this is not the case since fewer than half the number of rings are observed when introducing dye solution only after the NPoM constructs are assembled, suggesting limited migration of MB molecules towards the centre of the NPoM cavity. On-site reorientation of the MB dyes from in-plane (dark) to z-oriented (bright) could cause such revivals, but would be prevented by the well-defined CB[7] binding orientation (Fig.4d). Another hypothesis for the revivals are migrating Au adatoms that can trap light into picocavities close to single molecules (10, 48) or transient defects in the Au facets that depress the local plasma frequency resulting in large enhancements of electronic Raman emission (49). Such transient phenomena can also lead to the new SERRS peaks observed (Fig.S11), but will demand further enhancements of our spatiotemporal nanoscopy technique which is shot noise limited.

One intriguing test of our emitter position reconstruction method is to locate positions of molecules placed at known positions in the gap, for example using DNA origami (12, 43). However, our attempts to do this have shown that the DNA layer within the NPoM introduces a fluctuating background intensity and increases the gap thickness to ~5 nm, hence decreasing the dye signal intensity below the limit required for our spatial reconstruction imaging.

The construction of localised nano-lenses formed of plasmonic nanogaps supporting many highly-localised transverse modes does however for the first time offer a route to peer inside solvated molecule-metal interfaces under ambient conditions and resolves here how bleaching of molecules can be localised within a few nanometres. While in typical plasmonic constructs only a single mode controls emission, in all plasmonic narrow gap systems (such as dimers, patch antennas and these NPoMs) the multiple gap modes can clearly yield spatial information when the gap modes are well understood.

An intriguing scenario would be to use Au nano-constructs as nanolenses to reconstruct deep sub-wavelength images in real time to track the movement of emitters inside this nanogap. Because these nanogap quasi-normal modes form a complete basis set, improved localisation requires only broader spectral emission into many modes together with interferometry (imaging) in the far-field. However the symmetry of the currently facetted NPoMs or NP dimers leads to many modes being dark (m>2 states) which can limit azimuthal information (though broken by non-cylindrical symmetry of the NP (50)), while emission into these three antenna modes (the z-dipole in Fig.2c,e and x, y-dipoles in Fig.2d,f) limits direct Fourier imaging approaches without the basis state reconstruction discussed above. Approaches such as localisation microscopy (4) using frame-by-frame images of each photon emitted can be combined with the techniques here (as in Fig.4). Already these nanocavity gap modes can deliver nanometre precision from single frames for the location of single molecules, and resolve how multiple active emitters are distributed and change spatially over time.

Methods

Sample preparation

Sample preparation begins with fabrication of the gold mirror substrate by a template stripping process. A silicon wafer is coated with a thin layer of gold (100 nm) by thermal vapour deposition. A second silicon wafer is then scored with a diamond scribe and broken into many small pieces, which are then fixed to the gold surface on the first wafer using epoxy (Epo-Tek 377). After curing (by heating to 150 °C and then slowly cooling to room temperature) these pieces can be stripped off the first wafer as needed, by gentle application of shear force using a pair of tweezers. The gold surface on silicon freshly stripped in this manner is very clean and exceptionally flat (RMS roughness of 0.23 nm (38)). Silicon pieces still affixed to the gold layer on the first wafer can be stored at room temperature in air indefinitely, and stripped off as needed.

Fabrication of the nanoparticle on mirror structure with CB:MB host-guest complex is then carried out by preparing a 1 mM solution of MB and a 1 mM solution of CB and mixing these together, allowing encapsulation of the MB guest molecules inside the CB cavities. A freshly stripped piece of template-stripped gold is then allowed to soak in this solution overnight. Finally, a small droplet of citrate-stabilized gold nanoparticle solution (BBI Solutions) is then pipetted onto the prepared piece of template-stripped gold, and allowed to rest for a few seconds. Excess nanoparticles are flushed from the gold with de-ionized water, and the surface is blown dry with a nitrogen gun. Samples prepared in this manner can be stored under nitrogen flow for at least two weeks with little observed change in spectra or numbers of each emission shape (Fig.3g and supplementary Fig.S14-15).

Collection of spectra and far-field scattering profiles

Samples are studied using the experimental setup shown in supplementary Fig.S16 with a detailed description in Supplementary (Experimental Setup). Samples are illuminated with white light from a halogen lamp and are imaged in dark-field through a 100x dark field/bright field objective using a CCD camera. These dark-field images are used in conjunction with a motorized stage to automatically centre the view on a target nanoparticle for analysis. Computer vision and automation for this purpose are enabled by Python and the Open Source Computer Vision Library (OpenCV). After centring, a dark-field spectrum is taken under the same white light illumination using a fibre-coupled spectrometer (supplementary Fig.S5). A second, magnified, dark-field image of the target nanoparticle is taken on a second EMCCD camera using the zero order reflection of a grating monochromator after passing through a series of prefilters (Thorlabs FEL0650 and FES0750, supplementary Fig.S16) to limit collected light within the 650-750 nm wavelength range. The white light is then shuttered, and a radially-polarized HeNe laser is turned on, allowing excitation of the MB molecules in the sample at the pump wavelength of 633 nm. The emission is collected and imaged in the same configuration as the dark-field, using the zero order of the monochromator. Finally, the monochromator grating is rotated to first order, and the spectrum of the emission is collected. The computer then automatically moves the motorized stage to the next particle, and the process is repeated (hundreds of NPoMs in each single experiment). We note that the weak light emission from individual NPoMs of 1 kcts/mW/s integrated or 0.5 cts/mW/s/pixel in images, means that integration times of 10 s are required to adequately discriminate the different shapes, hence integrating over any more rapidly fluctuating phenomena such as the recently described picocavities (10, 48, 51).

COMSOL multiphysics simulations

The optical properties of the NPoM system are simulated using the finite element method (FEM) to solve Maxwell's equations (COMSOL Multiphysics v5.4). The gold nanoparticle is modelled as an 80 nm diameter sphere with a flat lower facet 20 nm in diameter. The permittivity of gold is modelled by a 2-pole Lorentz-Drude permittivity $\varepsilon(\mathbf{r};\omega) = \varepsilon_0\varepsilon_\infty\left(1 - \sum_{i=1}^{2}\omega_{p,i}^2/(\omega^2 - \omega_{0,i}^2 + i\omega\gamma_i)\right)$ where $\varepsilon_\infty = 6$, $\omega_{p,1} = 5.37 \times 10^{15}$ rad/s, $\omega_{0,1} = 0$ rad/s, $\gamma_1 = 6.216 \times 10^{13}$ rad/s, $\omega_{p,2} = 2.2636 \times 10^{15}$ rad/s, $\omega_{0,2} = 4.572 \times 10^{15}$ rad/s, $\gamma_2 = 1.332 \times 10^{15}$ rad/s. The gap spacer is modelled as a 1 nm-thick dielectric layer with refractive index 1.45 while the background material has a refractive index of 1.

In Fig.1, a point electric dipole emitter is placed in a NPoM gap at different radial coordinates, and the simulations are carried at a wavelength of 660 nm. The plasmonic nanogap cavity modes (Fig.2) are modelled as quasinormal modes (QNMs) described with complex eigenfrequencies. The QNMs are calculated by using QNMEig (36), an open source program based on COMSOL. The far-field emission patterns of the emitter and of each QNM are obtained by using RETOP (52), an open source code for Near-to-Far-Field Transformations (NFFT) of generalized guided waves. Finally, the outcoupling efficiency of each QNM is computed as the ratio of the far-field radiation power to the total dissipated power.

Author Contributions
MJH, OSO, WMD and JJB devised the experimental techniques and developed sample fabrication, MJH, WMD, RC, OSO developed the spectral analysis, NK, MJH, AD, OH, RC and JJB developed the simulations and analytic models, all authors contributed to writing the manuscript.

Conflicts of interest
The authors declare no conflicts of interest.

Corresponding author
Correspondence to J.J.B. (jjb12@cam.ac.uk)

References

1. A. F. Koenderink, A. Alu, A. Polman, Nanophotonics: shrinking light-based technology. *Science* **348**, 516–521 (2015).
2. S. A. Maier, *et al.*, Local detection of electromagnetic energy transport below the diffraction limit in metal nanoparticle plasmon waveguides. *Nat. Mater.* **2**, 229 (2003).
3. W. E. Moerner, L. Kador, Optical detection and spectroscopy of single molecules in a solid. *Phys. Rev. Lett.* **62**, 2535 (1989).

4. S. J. Sahl, S. W. Hell, S. Jakobs, Fluorescence nanoscopy in cell biology. *Nat. Rev. Mol. Cell Biol.* **18**, 685 (2017).

5. G. Vicidomini, P. Bianchini, A. Diaspro, STED super-resolved microscopy. *Nat. Methods* **15**, 173 (2018).

6. J. J. Baumberg, J. Aizpurua, M. H. Mikkelsen, D. R. Smith, Extreme nanophotonics from ultrathin metallic gaps. *Nat. Mater.*, 1 (2019).

7. S. Zhang, R. Geryak, J. Geldmeier, S. Kim, V. V. Tsukruk, Synthesis, assembly, and applications of hybrid nanostructures for biosensing. *Chem. Rev.* **117**, 12942–13038 (2017).

8. J.-F. Li, C.-Y. Li, R. F. Aroca, Plasmon-enhanced fluorescence spectroscopy. *Chem. Soc. Rev.* **46**, 3962–3979 (2017).

9. Y. B. Zheng, B. Kiraly, P. S. Weiss, T. J. Huang, Molecular plasmonics for biology and nanomedicine. *Nanomed.* **7**, 751–770 (2012).

10. F. Benz, *et al.*, Single-molecule optomechanics in "picocavities." *Science* **354**, 726–729 (2016).

11. W. Zhu, *et al.*, Quantum mechanical effects in plasmonic structures with subnanometre gaps. *Nat. Commun.* **7**, 11495 (2016).

12. O. S. Ojambati, *et al.*, Quantum electrodynamics at room temperature coupling a single vibrating molecule with a plasmonic nanocavity. *Nat. Commun.* **10**, 1049 (2019).

13. M. Kauranen, A. V. Zayats, Nonlinear plasmonics. *Nat. Photonics* **6**, 737 (2012).

14. M. Pelton, Modified spontaneous emission in nanophotonic structures. *Nat. Photonics* **9**, 427 (2015).

15. G. M. Akselrod, *et al.*, Probing the mechanisms of large Purcell enhancement in plasmonic nanoantennas. *Nat. Photonics* **8**, 835 (2014).

16. R. J. C. Brown, M. J. T. Milton, Nanostructures and nanostructured substrates for surface—enhanced Raman scattering (SERS). *J. Raman Spectrosc.* **39**, 1313–1326 (2008).

17. R. F. Aroca, Plasmon enhanced spectroscopy. *Phys. Chem. Chem. Phys.* **15**, 5355–5363 (2013).

18. B. Fu, B. P. Isaacoff, J. S. Biteen, Super-Resolving the Actual Position of Single Fluorescent Molecules Coupled to a Plasmonic Nanoantenna. *ACS Nano* **11**, 8978–8987 (2017).

19. M. Raab, C. Vietz, F. D. Stefani, G. P. Acuna, P. Tinnefeld, Shifting molecular localization by plasmonic coupling in a single-molecule mirage. *Nat. Commun.* **8**, 13966 (2017).

20. D. L. Mack, *et al.*, Decoupling absorption and emission processes in super-resolution localization of emitters in a plasmonic hotspot. *Nat. Commun.* **8**, 14513 (2017).

21. E. Wertz, B. P. Isaacoff, J. D. Flynn, J. S. Biteen, Single-Molecule Super-Resolution Microscopy Reveals How Light Couples to a Plasmonic Nanoantenna on the Nanometer Scale. *Nano Lett.* **15**, 2662–2670 (2015).

22. S. M. Stranahan, K. A. Willets, Super-resolution Optical Imaging of Single-Molecule SERS Hot Spots. *Nano Lett.* **10**, 3777–3784 (2010).

23. F. Balzarotti, F. D. Stefani, Plasmonics Meets Far-Field Optical Nanoscopy. *ACS Nano* **6**, 4580–4584 (2012).

24. B. de Nijs, *et al.*, Unfolding the contents of sub-nm plasmonic gaps using normalising plasmon resonance spectroscopy. *Faraday Discuss.* **178**, 185–193 (2015).

25. R. Chikkaraddy, *et al.*, Single-molecule strong coupling at room temperature in plasmonic nanocavities. *Nature* **535**, 127–130 (2016).

26. R. W. Taylor, *et al.*, Precise Subnanometer Plasmonic Junctions for SERS within Gold Nanoparticle Assemblies Using Cucurbit[n]uril "Glue." *ACS Nano* **5**, 3878–3887 (2011).

27. C. Carnegie, *et al.*, Mapping SERS in CB:Au Plasmonic Nanoaggregates. *ACS Photonics* **4**, 2681–2686 (2017).

28. J. F. Herrmann, C. Höppener, Dumbbell gold nanoparticle dimer antennas with advanced optical properties. *Beilstein J. Nanotechnol.* **9**, 2188–2197 (2018).

29. L. V. Brown, H. Sobhani, J. B. Lassiter, P. Nordlander, N. J. Halas, Heterodimers: Plasmonic Properties of Mismatched Nanoparticle Pairs. *ACS Nano* **4**, 819–832 (2010).

30. M.-W. Chu, *et al.*, Probing Bright and Dark Surface-Plasmon Modes in Individual and Coupled Noble Metal Nanoparticles Using an Electron Beam. *Nano Lett.* **9**, 399–404 (2009).

31. A. Rose, *et al.*, Control of Radiative Processes Using Tunable Plasmonic Nanopatch Antennas. *Nano Lett.* **14**, 4797–4802 (2014).

32. P. B. Joshi, T. P. Anthony, A. J. Wilson, K. A. Willets, Imaging out-of-plane polarized emission patterns on gap mode SERS substrates: from high molecular coverage to the single molecule regime. *Faraday Discuss.* **205**, 245–259 (2017).

33. C. Tserkezis, *et al.*, Hybridization of plasmonic antenna and cavity modes: Extreme optics of nanoparticle-on-mirror nanogaps. *Phys. Rev. A* **92**, 053811 (2015).

34. R. Chikkaraddy, *et al.*, How Ultranarrow Gap Symmetries Control Plasmonic Nanocavity Modes: From Cubes to Spheres in the Nanoparticle-on-Mirror. *ACS Photonics* **4**, 469–475 (2017).

35. N. Kongsuwan, *et al.*, Plasmonic nanocavity modes: From near-field to far-field radiation. *ArXiv191002273 Phys.* (2019) (October 25, 2019).

36. W. Yan, R. Faggiani, P. Lalanne, Rigorous modal analysis of plasmonic nanoresonators. *Phys. Rev. B* **97**, 205422 (2018).

37. C. Sauvan, J. P. Hugonin, I. S. Maksymov, P. Lalanne, Theory of the Spontaneous Optical Emission of Nanosize Photonic and Plasmon Resonators. *Phys. Rev. Lett.* **110**, 237401 (2013).

38. F. Benz, *et al.*, SERS of Individual Nanoparticles on a Mirror: Size Does Matter, but so Does Shape. *J. Phys. Chem. Lett.* **7**, 2264–2269 (2016).

39. J. Mertens, *et al.*, Tracking Optical Welding through Groove Modes in Plasmonic Nanocavities. *Nano Lett.* **16**, 5605–5611 (2016).

40. D. Vercruysse, *et al.*, Directional Fluorescence Emission by Individual V-Antennas Explained by Mode Expansion. *ACS Nano* **8**, 8232–8241 (2014).

41. A. G. Curto, *et al.*, Unidirectional Emission of a Quantum Dot Coupled to a Nanoantenna. *Science* **329**, 930–933 (2010).

42. Q. An, *et al.*, A general and efficient method to form self-assembled cucurbit[n]uril monolayers on gold surfaces. *Chem. Commun.*, 1989–1991 (2008).

43. R. Chikkaraddy, *et al.*, Mapping Nanoscale Hotspots with Single-Molecule Emitters Assembled into Plasmonic Nanocavities Using DNA Origami. *Nano Lett.* **18**, 405–411 (2018).

44. A. Delga, J. Feist, J. Bravo-Abad, F. J. Garcia-Vidal, Quantum Emitters Near a Metal Nanoparticle: Strong Coupling and Quenching. *Phys. Rev. Lett.* **112**, 253601 (2014).

45. R.-Q. Li, D. Hernángomez-Pérez, F. J. García-Vidal, A. I. Fernández-Domínguez, Transformation Optics Approach to Plasmon-Exciton Strong Coupling in Nanocavities. *Phys. Rev. Lett.* **117**, 107401 (2016).

46. A. L. Koner, W. M. Nau, Cucurbituril Encapsulation of Fluorescent Dyes. *Supramol. Chem.* **19**, 55–66 (2007).

47. W. M. Nau, J. Mohanty, Taming fluorescent dyes with cucurbituril. *Int. J. Photoenergy* (2005) https:/doi.org/10.1155/S1110662X05000206 (June 27, 2019).

48. M. Urbieta, *et al.*, Atomic-Scale Lightning Rod Effect in Plasmonic Picocavities: A Classical View to a Quantum Effect. *ACS Nano* **12**, 585–595 (2018).

49. Carnegie, C. et al., Flickering nm-scale disorder in a crystal lattice tracked by plasmonic 'flare' light emission. *under review Nat. Commun.* (2019).

50. M.-E. Kleemann, *et al.*, Revealing Nanostructures through Plasmon Polarimetry. *ACS Nano* **11**, 850–855 (2017).

51. C. Carnegie, *et al.*, Room-Temperature Optical Picocavities below 1 nm3 Accessing Single-Atom Geometries. *J. Phys. Chem. Lett.* **9**, 7146–7151 (2018).

52. J. Yang, J.-P. Hugonin, P. Lalanne, Near-to-Far Field Transformations for Radiative and Guided Waves. *ACS Photonics* **3**, 395–402 (2016).

Supplementary Information

Nanoscopy through a plasmonic nano-lens

Matthew J Horton[1], Oluwafemi S Ojambati[1], Rohit Chikkaraddy[1], William M Deacon[1], Nuttawut Kongsuwan[2], Angela Demetriadou[2,3], Ortwin Hess[2], Jeremy J Baumberg[1]

[1] NanoPhotonics Centre, Cavendish Laboratory, Department of Physics, JJ Thompson Avenue, University of Cambridge, Cambridge, CB3 0HE, UK
[2] Blackett Laboratory, Imperial College London, South Kensington Campus, London, SW7 2AZ, UK
[3] School of Physics and Astronomy, University of Birmingham, Birmingham, B15 2TT, UK

Methods: Simulations of a dipole emitter in a NPoM

A) FEM

In the FEM simulations performed using COMSOL, the optical fields are recorded on a two-dimensional plane in the space domain at a distance Δz=150 nm above the mirror surface. These fields are then propagated into the far-field and projected into real-space using a plane-wave approximation, accounting for the effects of the collection optics. This is done by first taking the discrete Fourier transform of the complex recorded field $E(x, y)$, in order to obtain an image of the field in the spatial frequency domain.

This result is then multiplied by $\exp\{i(-\Delta z)k_z(x, y)\}$, where $k_z(x, y) = \sqrt{(2\pi/\lambda)^2 - k_x^2 - k_y^2}$ in order to obtain the spatial frequency domain image of the field in the focal plane of the objective. In order to account for the numerical aperture of the objective, this result is multiplied by a k-plane mask $\frac{1}{2}\left(1 - \tanh\left(\left(\sqrt{k_x^2 + k_y^2} - k_c\right)/k_s\right)\right)$, where $k_c = (2\pi/\lambda)\sin(50°)$ and $k_s = 0.1k_c$, before taking the inverse Fourier transform to recover the fields at the detection plane (in the spatial domain). The squared norm of these fields then yields the images shown in Fig.1b and supplementary Fig.S3.

1B) FDTD

To confirm the COMSOL results, the CB:MB in NPoM system is also simulated using a finite-difference time-domain Maxwell solver (Lumerical FDTD). The simulation is set up assuming an 80 nm spherical nanoparticle with a 20 nm diameter circular bottom facet. Material data used for the gold is taken from Johnson and Christy, and the CB:MB layer is assumed to have a refractive index of 1.4 and a thickness of 0.9 nm.

Simulations of an 80 nm spherical NPoM with a flat bottom facet of a range of sizes between 0 nm and 34 nm are designed to replicate as closely as possible the system used in the experiments. Dimensions of the particle, particle facet, and gap size are set correspondingly, and complex wavelength-dependent refractive indices are selected to match each material used. To simulate a molecule emitting in the NPoM gap, we use a broad-spectrum vertically-oriented dipole source placed in the plasmonic hot-spot. The same filtering applied to the results of the COMSOL simulations is then applied here in order to obtain the images shown in supplementary Fig.S1.
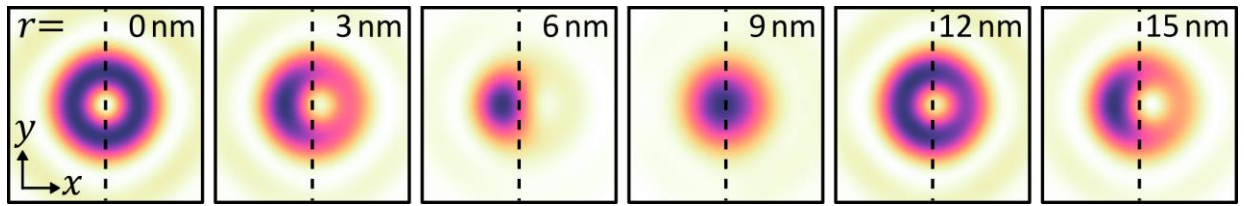
Fig.S1 | Far-field real-space images (normalized) simulated using FDTD after collection through an 0.9NA objective. The images confirm those obtained using the FEM method (Fig.1b).

Recovering emitter position from dark field and photoluminescence images

The method used to localize a single emitter within the cavity of each NPoM is derived from the results of modelling the NPoM structure numerically. This is done using either the FDTD model produced in Lumerical, or using the FEM model produced in COMSOL. The emitter positions obtained from either model agree to within <1 nm for emitter positions within a radial coordinate r<10 nm of the cavity centre. For emitter positions beyond 9 nm of the cavity centre, the emission intensity drops off rapidly for most NPoM geometries (supplementary Fig.S3). The spatial distribution of the emission here begins to resemble that observed at smaller values of r (supplementary Fig.S3 r=15 nm vs 3 nm) and hence it becomes less possible to unambiguously determine the position of the emitter. However since such highly displaced emitters give very weak light intensities, this has little effect on our results.

The procedure for extracting the position of a single emitter under each NPoM is outlined in supplementary Fig.S2.
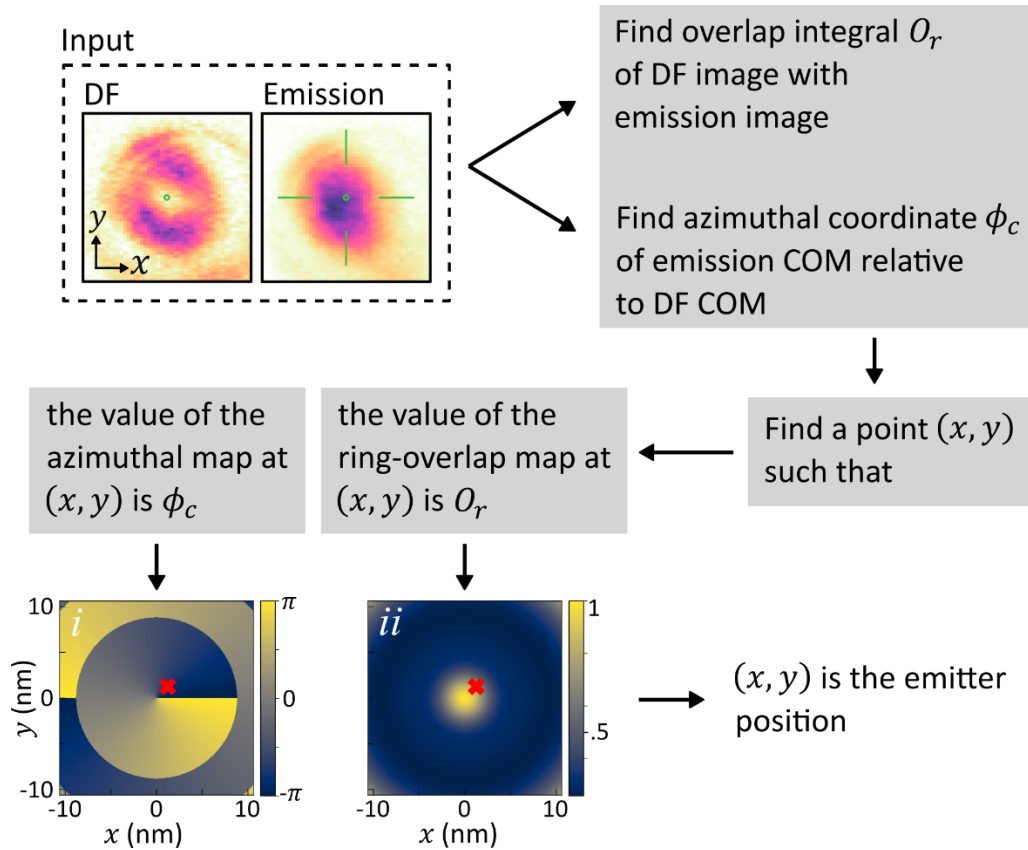
Fig.S2 | Methodology for recovering the position of an emitter in the NPoM gap using image of dark field scattering and image of the light emission (PL). The overlap integrals of a ring shaped distribution with the distributions obtained from emitters placed at different distances from the centre of the NPoM gap are computed using COMSOL simulations. These are used to generate a map where the radial coordinate of the emitter can be looked up given the same overlap integral calculated using experimental data. The azimuthal coordinate is simply obtained from the azimuth of the offset of the centre of mass of the PL image relative to the centre of mass of the dark field image.

First, the centre of mass of both the DF and the emission images is computed. The azimuthal coordinate of the emission centre of mass relative to the dark field centre of mass is then compared against an interpolated lookup table of the azimuthal coordinates for different emitter positions, generated from the simulation results. This yields the azimuthal coordinate of the emitter. Then, utilizing the fact that the DF spatial distribution of a NPoM is always ring-like, the overlap integral of the DF and emission is computed, and used as a measure of the degree to which the NPoM emission is ring-like (vs. spot-like). As before, this value is compared against an interpolated lookup table generated from the simulation results. This yields the radial coordinate of the emitter, completing the localization process.

The azimuthal lookup table $\phi_c(x, y)$ is generated from the simulations by taking the x coordinate of the centre of mass of the calculated emission image ($x_c(x)$) for a few dipole positions (at x=0, 3, 6, 9, 12, and 15 nm as shown in Fig.1b) along the positive x-axis (corresponding to a dipole azimuthal coordinate ϕ_d=0°). $x_c(x)$ is then linearly interpolated and passed through a threshold filter yielding 1 for $x_c \leq 0$ and 0 for $x_c > 0$, thus indicating the domains where the emission beaming is in the direction respectively opposite or identical to the direction of displacement of the dipole. The values of the lookup table on the positive x-axis are then assigned to $\xi_c(x_c)$=180° wherever $x_c \leq 0$ and $\xi_c(x_c)$=0° wherever $x_c > 0$. Finally, the rest of

the lookup table is filled exploiting the cylindrical symmetry of the NPoM geometry, by simply adding the azimuthal coordinate of the dipole $\phi_d(x, y) = \tan^{-1}(y/x)$ to the values of $\xi_c(x_c)$, so that $\phi_c(x, y) = \tan^{-1}(y/x) + \xi_c\left(\sqrt{x^2 + y^2}\right)$.

The ring-overlap map $O_r(x, y)$ is similarly generated from the simulations by first computing O_r^{x+} at each of the dipole positions simulated (x=0, 3, 6, 9, 12, and 15 nm) on the positive x-axis. The method consists of taking the ring shaped emission image I_{ring} at x=0 (leftmost image in Fig.1b) and a second image $I_{emission}$ from among those in Fig.1b and computing:

$$O_r = \frac{1}{N} \sum_{u,v} \frac{I_{emission}(u, v)}{\max\limits_{u,v} I_{emission}(u, v)} I_{ring}(u, v)$$

where

$$N = \frac{1}{\max\limits_{u,v} I_{ring}(u, v)} \sum_{u,v} I_{ring}(u, v)^2$$

and u, v are the image coordinates in pixels. This is done taking $I_{emission}$ to be each of the images in Fig.1b in turn. The remaining values of O_r^{x+} are found by interpolation using a cubic spline. The full lookup table $O_r(x, y)$ is then filled by again exploiting the cylindrical symmetry of the NPoM geometry, and simply rotating O_r^{x+} about $(x, y) = (0,0)$.

COMSOL simulation of emission profile for various facet sizes

FEM simulations using COMSOL for a large range of facet sizes and emitter positions reveal a consistent drop-off in integrated emission intensity for emitter positions greater than 10 nm away from the centre of the NPoM cavity. Furthermore, the emission profile of a centred emitter is always a ring, and always evolves into a spot at a distance within 3 to 9 nm from centre. For facet sizes greater than 20 nm, there exists a limiting radius to the emitter position beyond which the emission profile reverts from spot to ring (around 12 nm for all facet sizes >20 nm). In all cases this reversion occurs for an emitter position with an integrated intensity <30% of that at the maximally out-coupled position.

The emitter position recovery procedure outlined in Fig.S2 depends on the facet size being known a priori, which can be extracted by suitably fitting the peak positions of the dark field scattering (eg Fig.4e with Fig.2a). From the $3 < r < 9$ nm region of Fig.S3, we see that, around w = 20 nm, changes in facet size of 10 nm result in far-field pattern shifts equivalent to dipole position shifts of at most 2 nm. We can therefore conclude that achieving an accuracy in the recovered emitter position of ± 1 nm requires knowledge of the facet size to within ± 5 nm, which gives easily measurable peak shifts in the dark field.
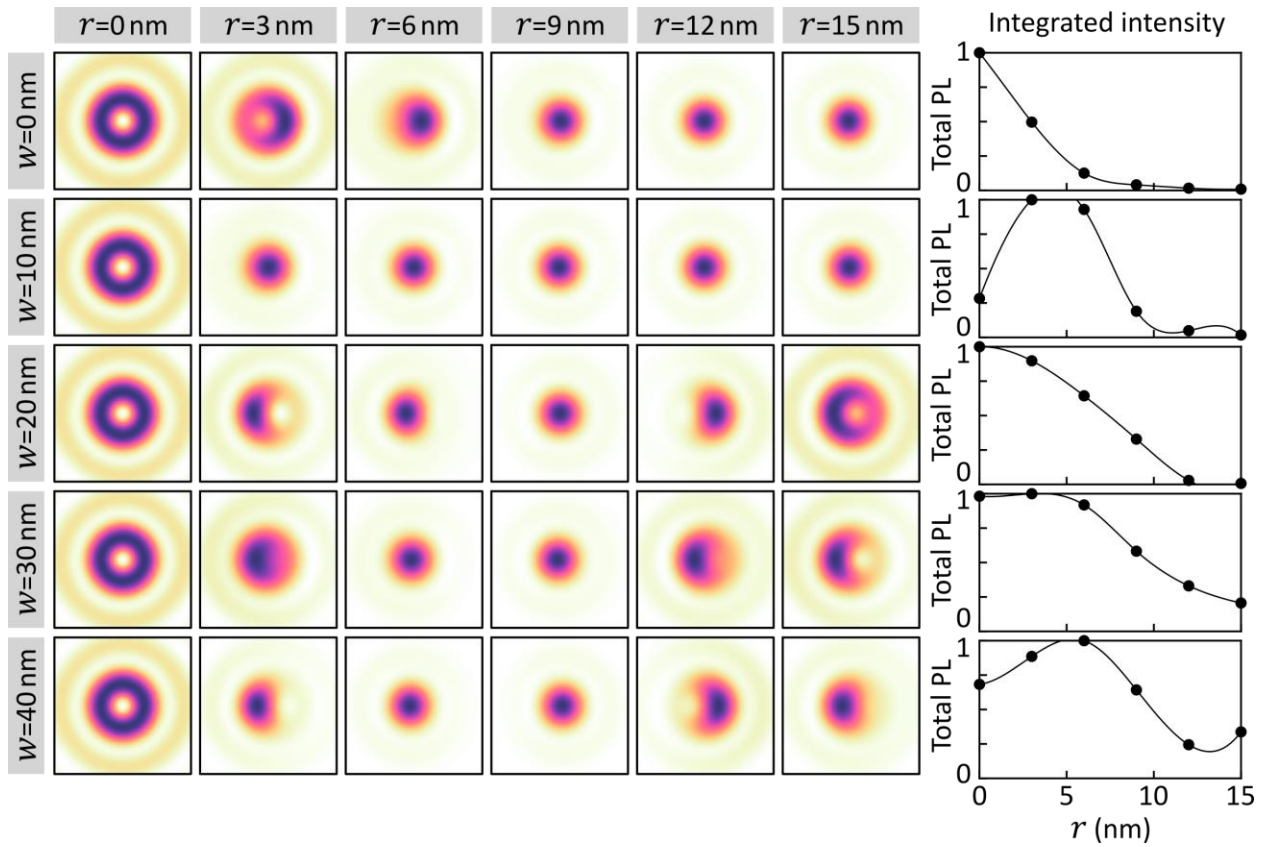
Fig.S3 | Simulations of emission profile at λ=660 nm for various facet sizes (left) and emitter positions (top). Integrated emission intensity (right) shown as a function of emitter position at each facet size.

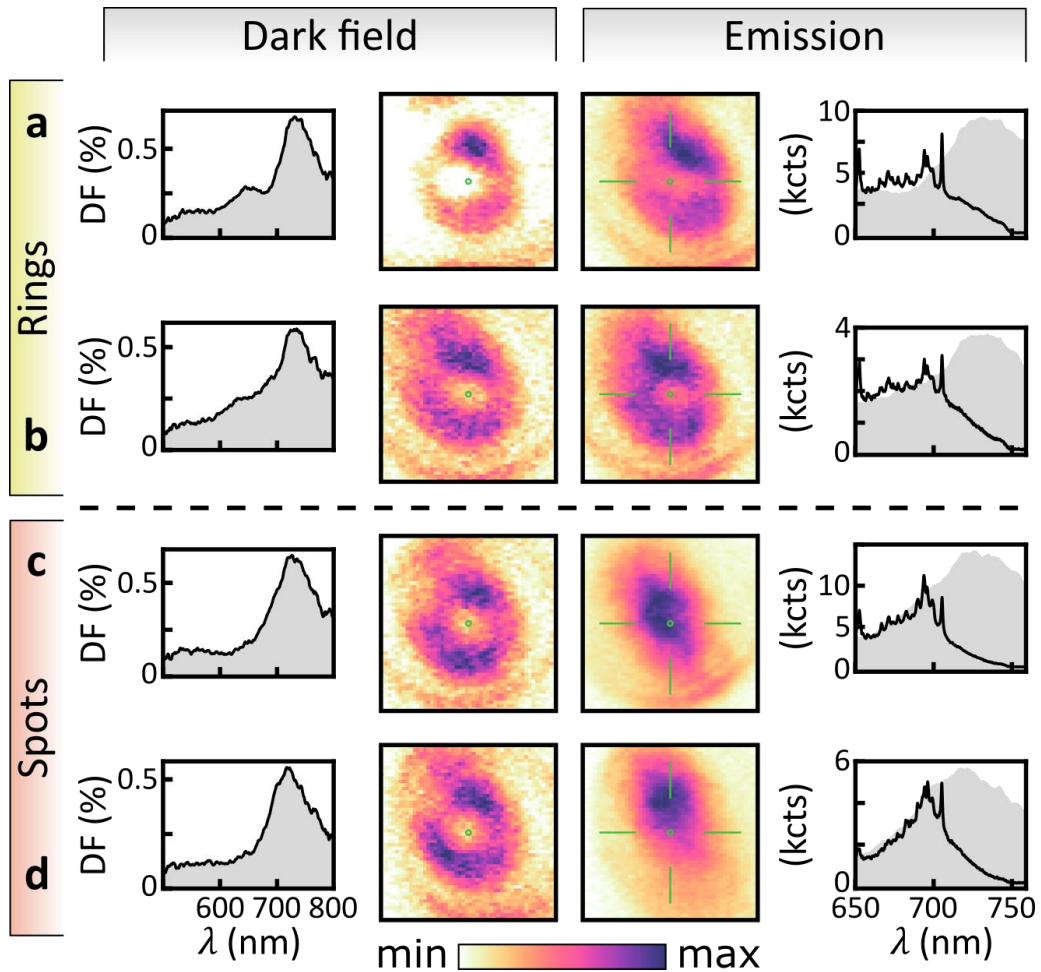Additional examples of NPoM emission profiles

Fig.S4 | **Additional examples of far-field emission profiles to compare with Fig.5. a, NPoMs with ring shaped emission and b, NPoMs with spot shaped emission.**
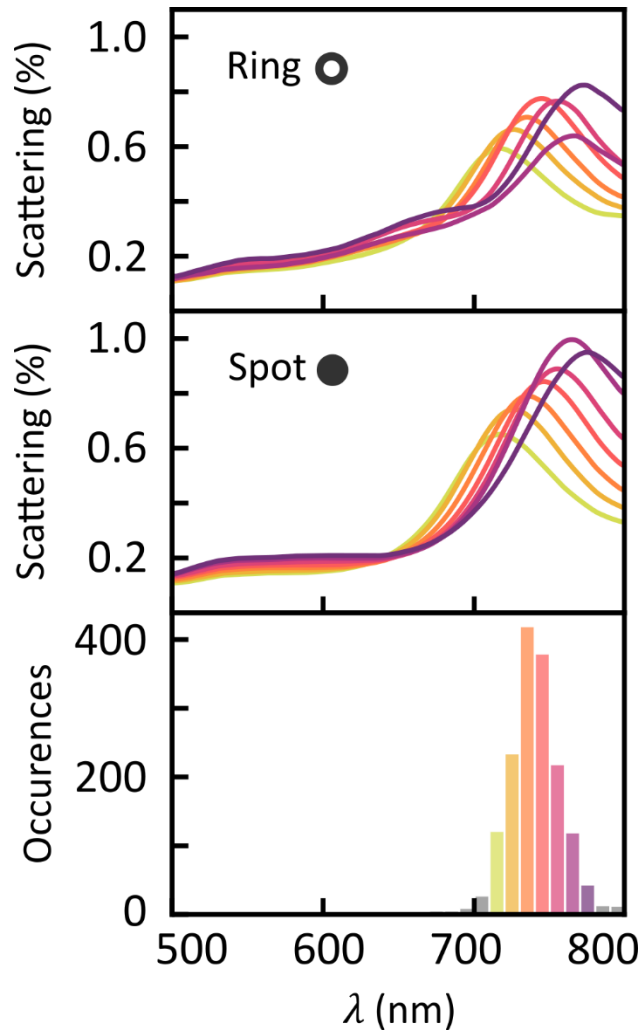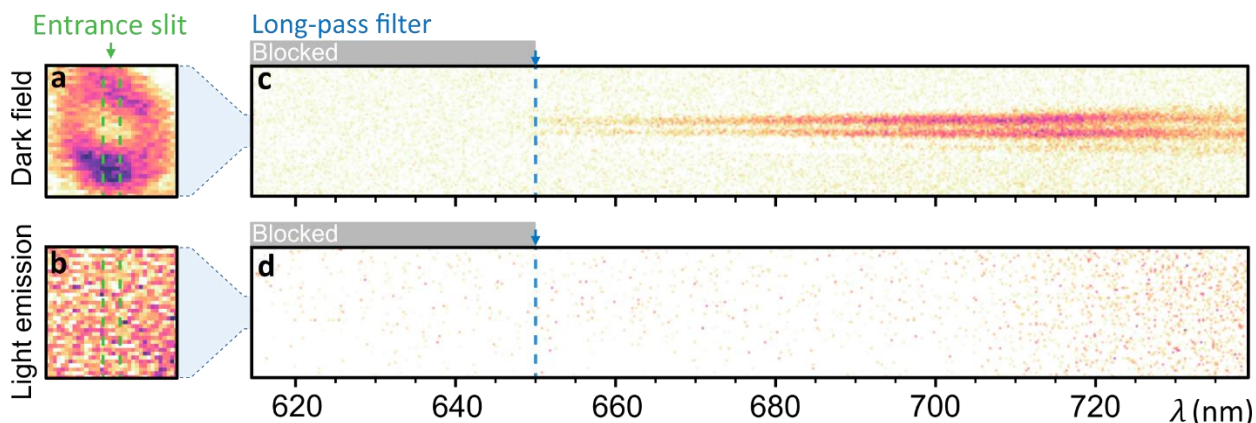
DF Spectra

Fig.S5 | Averaged DF spectra of 1602 NPs, separated by light emission image shape into the 201 rings (top) and 1189 spots (middle), binned by the spectral position of their largest DF spectrum peak (bottom). Coloured lines are the averaged DF spectrum of NPs in the bin of the corresponding colour.

Emission from NPoMs prepared with CB[7] only

Fig.S6 | DF and light emission from a 80 nm Au NPoM with a molecular spacer consisting of CB[7] molecules without the addition of any dye molecules.

If a substrate of template stripped gold prepared initially with CB[7] but omitting the MB is used to build NPoMs from 80 nm gold nanoparticles using the usual drop-casting method, no emission is observed in most nanoparticles (supplementary Fig.S7a,c). The few particles in the sample that exhibit some form of weak emission have spot-like spatial distributions (supplementary Fig.S7b). This weak emission is most likely from electronic Raman scattering from the Au nanoparticle and it is 10-20 times weaker than the peak PL emission with dyes in the gap.
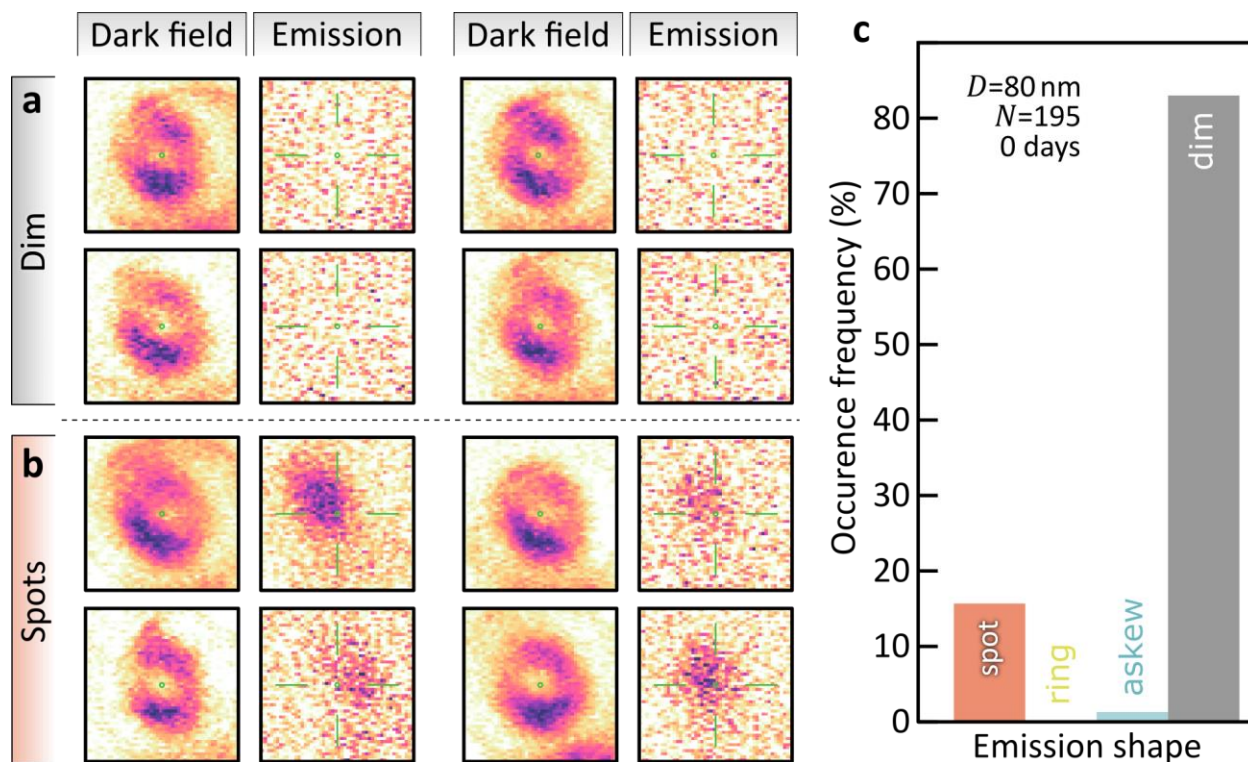
Fig.S7 | Far-field emission profiles of 80 nm Au NPoMs prepared with CB[7], but without MB dyes. a, Dark field and emission spatial profiles for four different nanoparticles exhibiting no emission or b, very weak spot-like emission. c, Percentage ratio of each distribution observed.

Time evolution of NPoM emission profile

An example of the time evolution of the intensity and angular distribution of NPoM emission was given in Fig.4. This evolution is subtly different for different NPoMs, with some exhibiting a greater or lesser number of revivals in emission intensity over time. This can be seen in the following additional examples (supplementary Fig.S8-10):
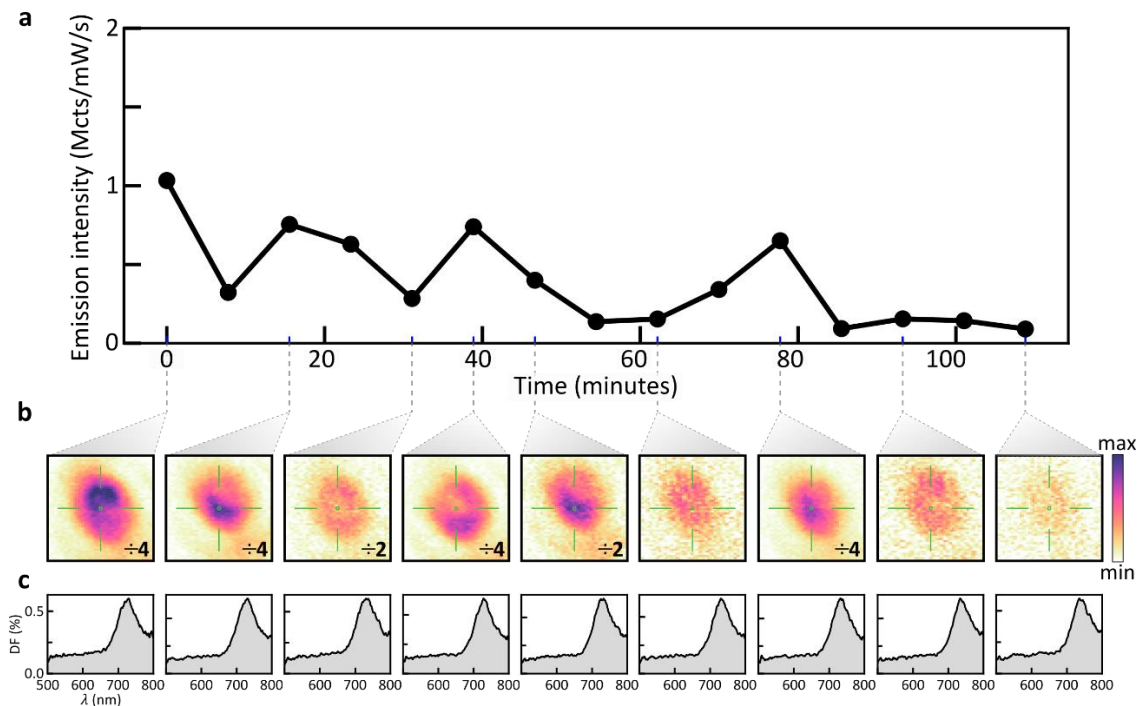
Fig.S8 | Time evolution of real-space emission from a single 80 nm NPoM (additional example #1). a, Integrated intensities vs time. **b,** Corresponding real-space spectrally-filtered emission images at times as marked, with the reticle showing the position of the dark-field ring centre. Integration times are 10 s, for 633 nm laser. **c,** DF spectra at the times marked in b.
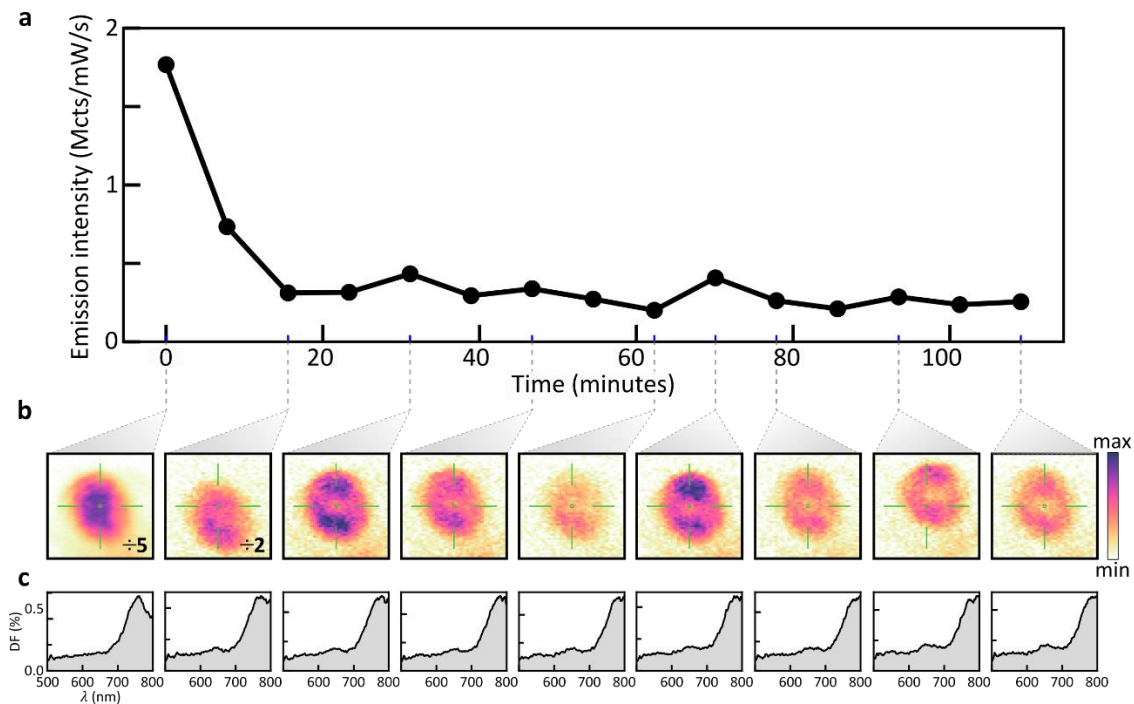
Fig.S9 | Time evolution of real-space emission from a single 80 nm NPoM (additional example #2). a, Integrated intensities vs time. **b,** Corresponding real-space spectrally-filtered emission images at times as marked, with the reticle showing the position of the dark-field ring centre. Integration times are 10 s, for 633 nm laser. **c,** DF spectra at the times marked in b.
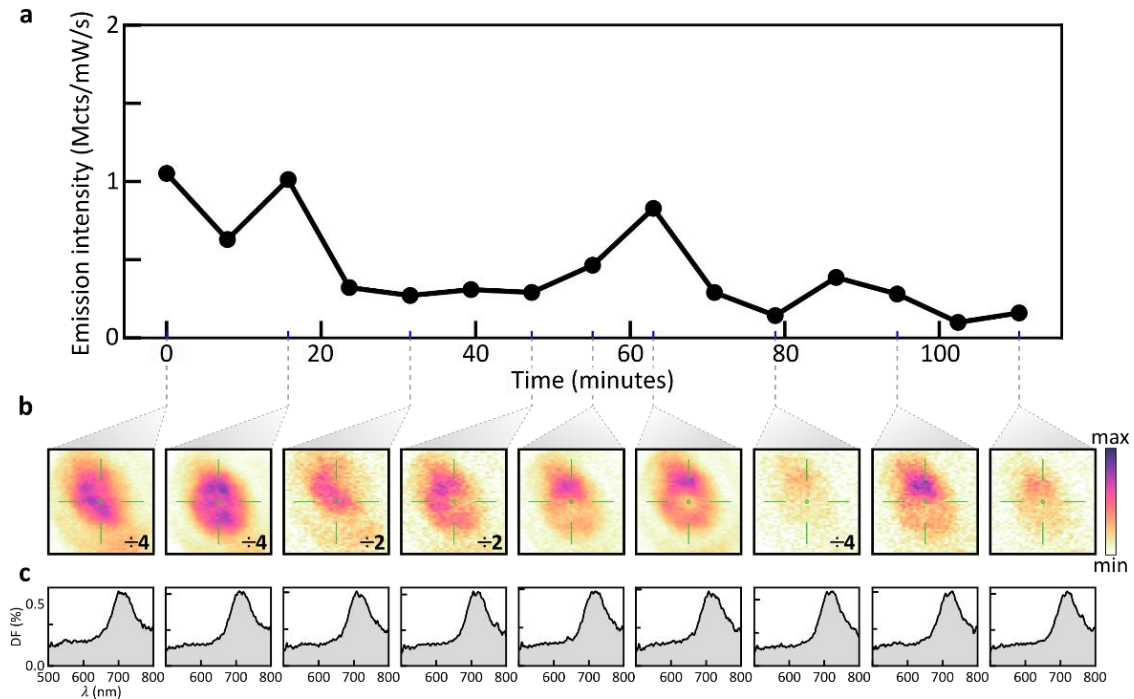
Fig.S10 | Time evolution of real-space emission from a single 80 nm NPoM (additional example #3). a, Integrated intensities vs time. **b,** Corresponding real-space spectrally-filtered emission images at times as marked, with the reticle showing the position of the dark-field ring centre. Integration times are 10 s, for 633 nm laser. **c,** DF spectra at the times marked in b.

## Time evolution of emission spectra
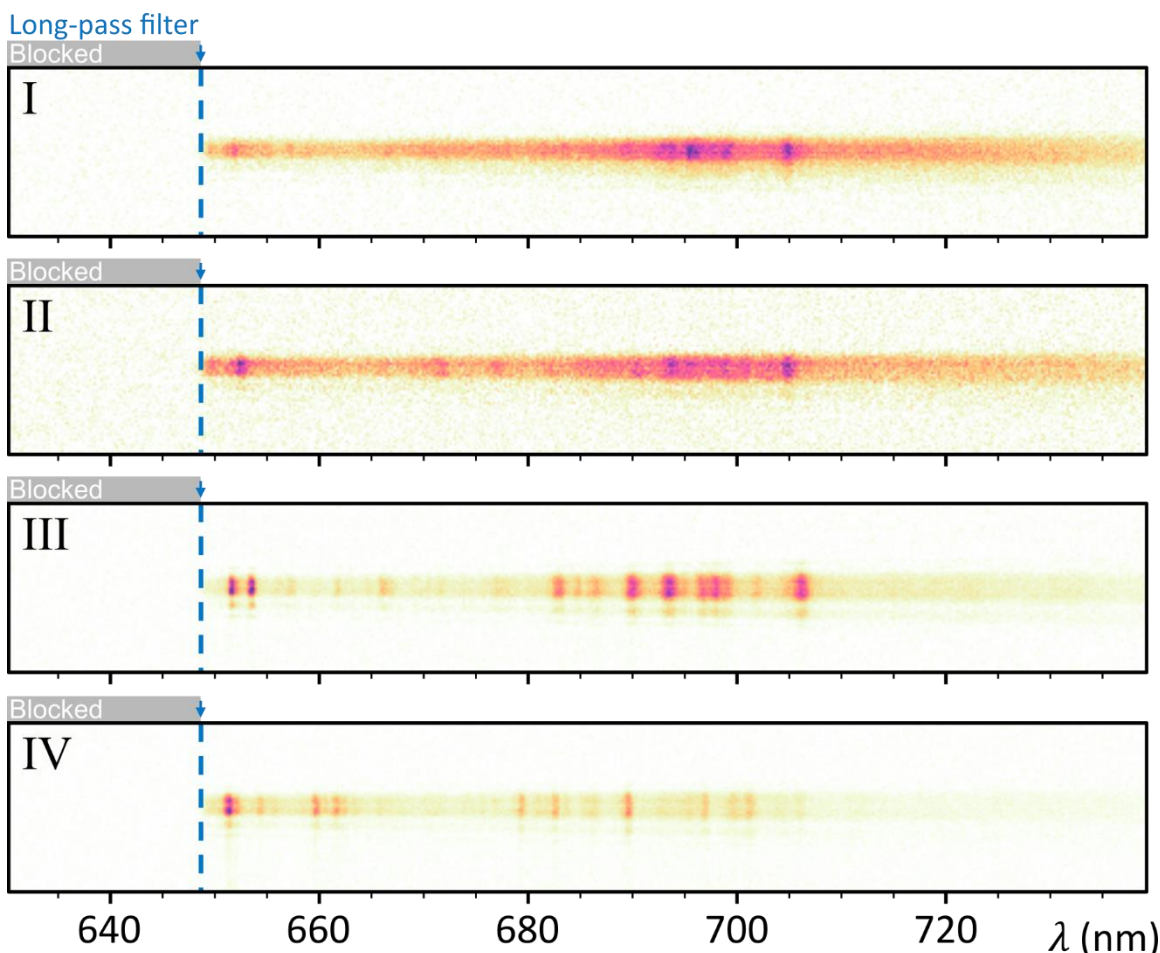
Fig.S11 | Evolution of emission spectra from a single NPoM under continuous illumination. Spectra shown are taken concurrently with the data in Fig.4, with I-IV corresponding to images & time given there. A 650 nm long-pass filter blocks all emission below 650 nm, including the excitation wavelength at 633 nm.

Supplementary Fig.S11 shows the emission spectra of the NPoM imaged in Fig.4 at four arbitrarily selected moments in time. Many of the spectral peaks observed over the course of observing this particle are consistent with the Raman spectrum of the MB dye, but shift in both position and intensity over time. One hypothesis to explain this is the migration of Au adatoms in the facet forming picocavities close to single molecules (1, 2) leading to a transient increase in the confinement of light to the molecule's vicinity. Another is the rearrangement of Au atoms within the NPoM facets (3) resulting in transient defects at the grain boundaries, which enhance the SERRS of nearby molecules (see main text discussion).

Simulations of multiple dipoles in a NPoM

Generating the far-field scattering profile for a NPoM hosting two or more molecular emitters within its plasmonic hot spot can be achieved by suitably combining the optical fields in the far-field from different emitters at different locations.
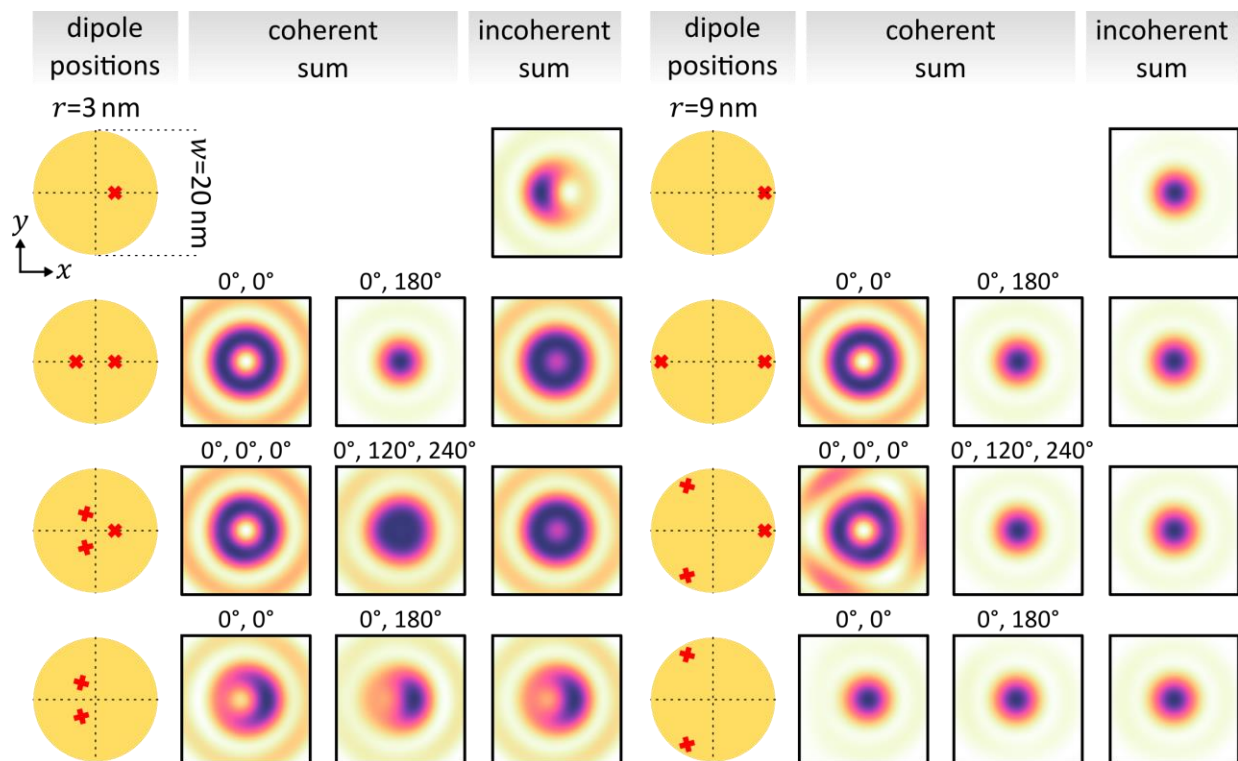
Fig.S12 | Resulting emission from 1,2,3 dipole places at r=3 or r=9 nm, when coherently summed with phases as marked, or incoherently summed.

Results of a few such combinations (Fig.S12) show how the asymmetric patterns are rapidly wiped out in both coherent and incoherent sums. As a result, it is not possible to uniquely quantify if the emitting multiple dipoles are coherently locked (as in a nanocavity polaritonic state) or independently incoherent.
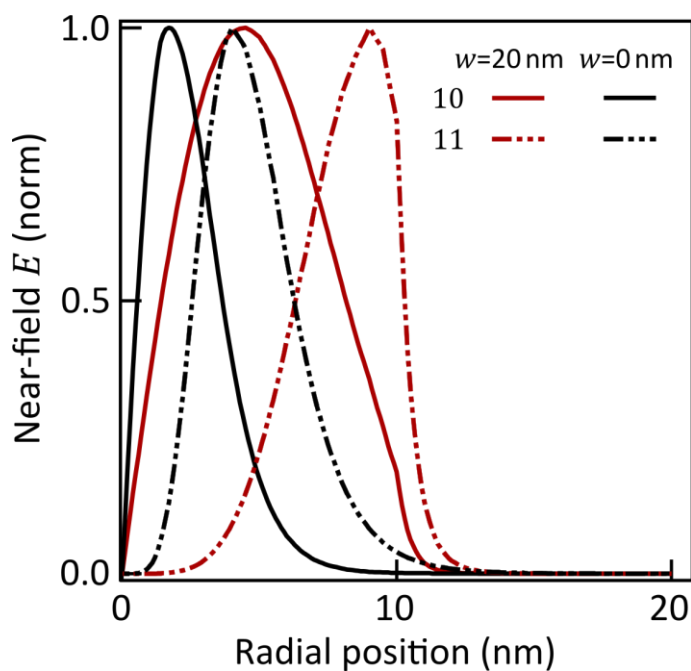
Mode coupling at different radial positions

Fig.S13 | Normalised near-field mode amplitude density *vs* radial coordinate for the (10) and (11) modes in the gap of a 80 nm NPoM with either facet size of *w*=0 nm (black) or 20 nm (blue). This shows the integrated near-field amplitude at each radial position.

Preservation of samples under nitrogen

Experiments studying the number of each type of far-field scattering distribution are repeated using two different samples, to explore aging. The second sample gave the same result as the first, revealing no change in the numbers of each type (supplementary Fig.S14, compare with first sample in Fig.3g). The average integrated emission intensity of nanoparticles in this sample are also observed to be stable for the full duration of the experiments.
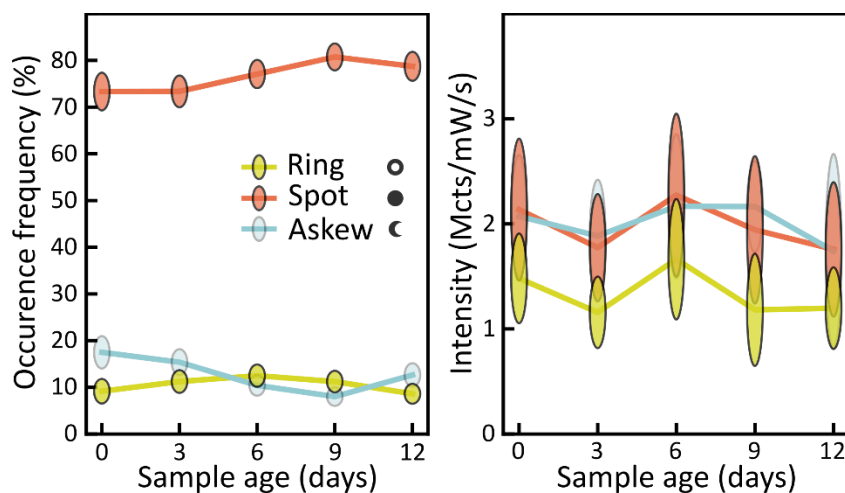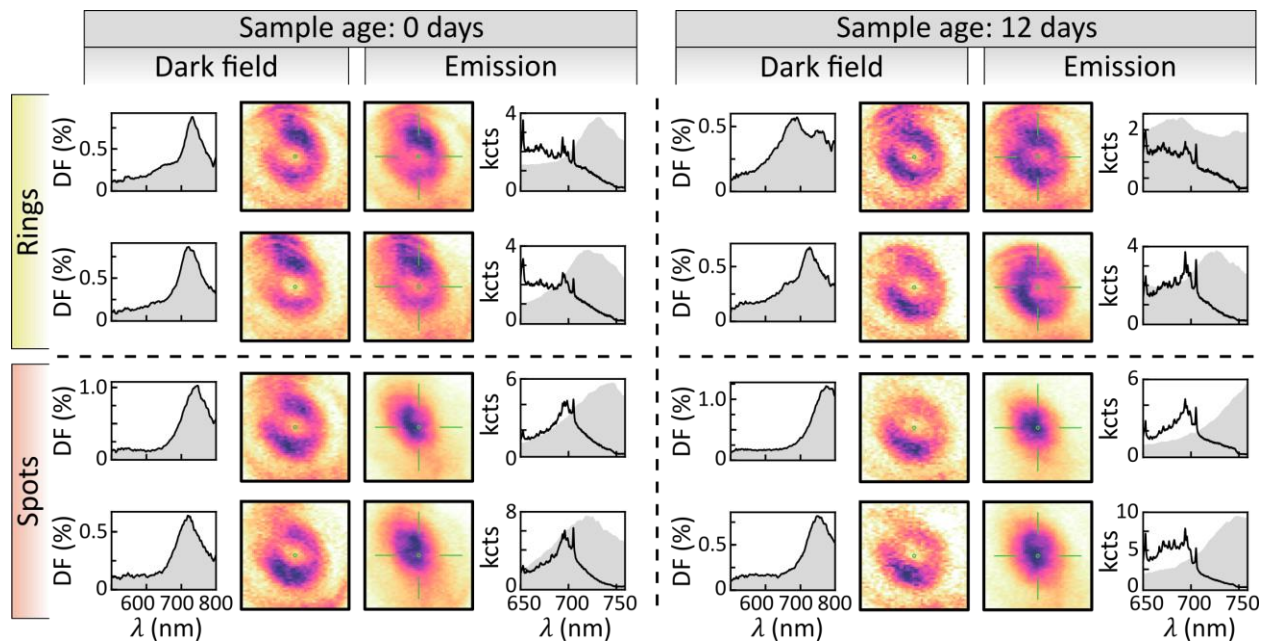

Fig.S14 | Long term time evolution of emission profile occurrence rates and integrated emission intensities for sample stored under nitrogen flow. The samples remain stable in storage for more than 12 days.
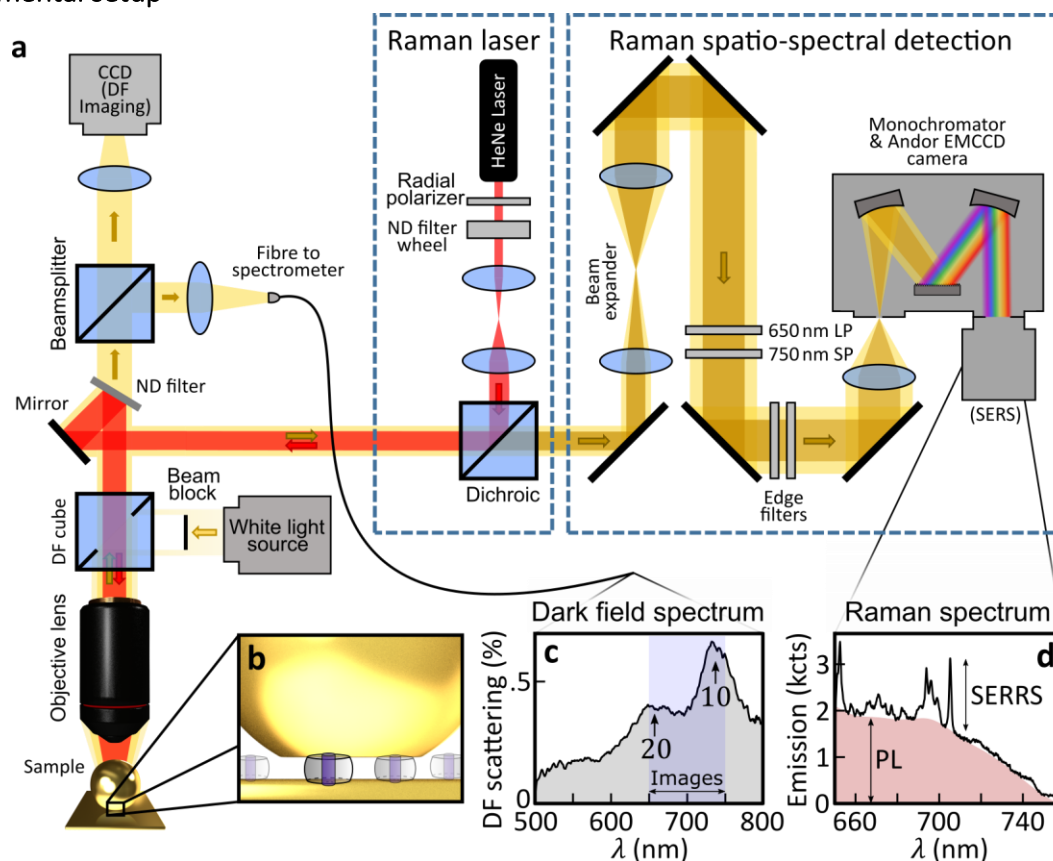
Emission and dark field spectra are likewise observed to be stable in samples stored for more than 12 days (supplementary Fig.S15).

Fig.S15 | Dark field and emission spectra before and after 12 days storage.

Experimental setup

Fig.S16 | Experimental setup. a, Schematic of both imaging and spectroscopy. Left side shows imaging system used for alignment, automatic sample scanning, and collection of DF spectra. Boxed section 'Raman laser' shows radially-polarized 633 nm excitation laser used in collection of emission images and spectra. Boxed section 'Raman spatio-spectral detection' shows separation of emission from excitation, magnification stages, imaging, and collection of emission spectra. b, Schematic of typical NPoM, with a flat facet and a CB[7] spacer layer (not to scale). c, Dark field scattering spectrum of a typical NPoM with a ring-shaped emission and d, emission spectrum.

The experimental setup can be subdivided into three distinct parts. The first consists of an imaging microscope (Olympus BX51) equipped with a motorized stage (Prior Scientific H101) upon which the NPoM samples are placed. The samples are illuminated and imaged through a 100x bright field/dark field objective (Olympus, numerical aperture of 0.9), with either laser illumination or white light from a halogen lamp. A dark field (DF) cube and circular beam block are used in conjunction with the halogen lamp to illuminate the sample only at high angles for DF imaging. A reflective neutral density filter (Thorlabs ND503A, optical density of 0.3) is used in transmission as a broadband non-polarizing 50:50 beamsplitter. The ND filter directs part of the transmitted light to an imaging charge-coupled camera (Lumenera Infinity3-1) to view the sample, and to a fibre-coupled spectrometer (Ocean Optics QEPRO) for dark field spectroscopy. A cube beamsplitter (60:40 R:T) distributes light between these the imaging camera and the dark field spectrometer. The same reflective ND filter is used in reflection to both guide laser illumination towards the sample, and for directing emission towards the spatio-spectral detection system.

The second part of the setup is the Raman laser system used to excite the NPoM samples. It consists of an automatically shuttered HeNe laser (Thorlabs HNL210L, emission wavelength at 633 nm) directed through a radial polarization converter (Altechna RPC-632-04 S-waveplate). A computer controlled ND

filter wheel is used for power control, a beam expander with a magnification of 10x, and a dichroic beamsplitter used to direct the radially polarized laser towards the main experimental setup, and to direct collected emission towards the final part of the setup.

The spatio-spectral detection system consists of a telescope (magnification 10) formed with two plano-convex lenses. This is followed by a sequence of filters chosen to block the excitation wavelength and limit detection to the desired wavelength range by using a long pass filter (Thorlabs FEL0650, cut-off wavelength at 650 nm) and a short pass filter (Thorlabs FES0750, cut-off wavelength at 750 nm). After magnification and filtering, the remaining light is focused onto the slit of a monochromator (Andor Shamrock SR-303i), where it is directed to an electron-multiplying CCD camera (Andor Newton 970 EMCCD) using either the zero order of the grating monochromator if images are desired, or using the first diffraction order when spectra are desired.

Note: Effect of gap size on emission
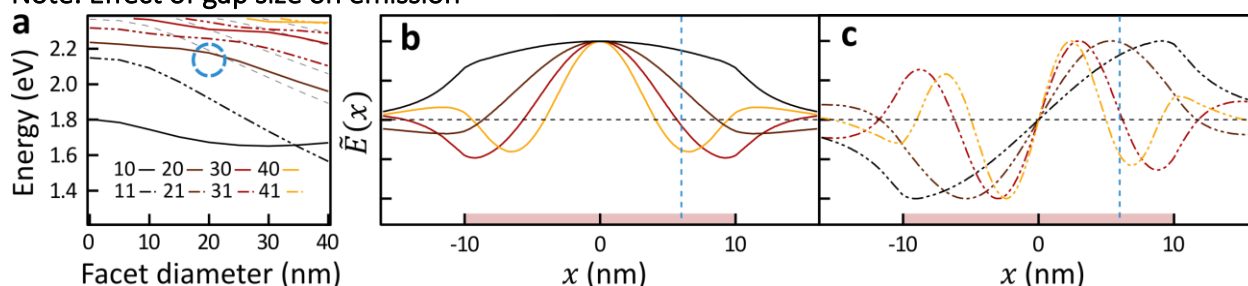
Fig.S17 | Plasmonic nanogap cavity modes of 80 nm NPoM with 2 nm gap and 20 nm facet diameter. a, Mode energies for the first 4 symmetric [solid lines (lm)=(10)-(40)] and asymmetric [dashed (11)-(41)] nanogap modes. Blue circle marks regime for facets of a typical $D{\sim}80$ nm NPoM. **b,c,** Corresponding near-field mode amplitudes with a 20 nm facet (normalised, colours as in a, dashed vertical at x=6 nm, extent of facet indicated by a pale red bar on the x-axis).

The CB[7] spacer layer used in the experimental portion of this paper precisely fixes the gap separation to 0.9 ± 0.05 nm.(4) However, similar far field emission images are found theoretically for larger gap sizes. In such a case, the mode energy positions shift (see maps in (5), and Fig.S17), and thus so does the mode mixing. This is very similar to the use of different NP sizes (Fig.3e,f). Despite these changes, the evolution of the emission spatial image as the emitter is moved away from centre remains very similar (a ring is observed for a centred emitter, and emission becomes more spot-like as the emitter is shifted away from centre, as shown in Fig.S18). As a result, dye position reconstruction remains feasible for larger gap sizes.
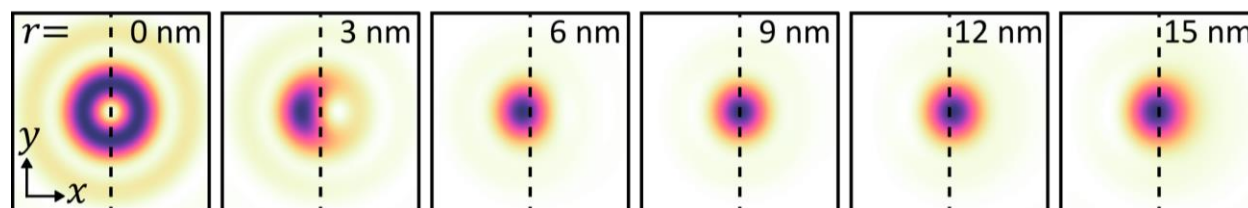
Fig.S18 | Far-field real-space images (normalized) simulated using FEM after collection through an 0.9NA objective, using the same structure and dimensions as in Fig.1b except with a 2 nm gap thickness instead of 1 nm.

Note: Mode nomenclature

In this article, the QNMs of the NPoM are labelled in order of increasing energy as lm = 10, 11, 20, 21, 22, 30, 31, 32, 33… where l and m are indices analogous to those of the spherical harmonics $Y_l^m(\theta, \phi)$ (see for example (6)). This nomenclature was chosen as it closely reflects the distribution of charge on the surface of a NPoM for each mode. Note the lm = 00 mode is intentionally left out as it represents the case of the NPoM accumulating or dissipating charge, which is not possible to excite for a NPoM on an electrically insulating spacer layer such as the CB:MB layers used here. Modes with even m radiate into a ring-shaped far-field spatial distribution, whereas modes with odd m radiate into spot-shaped far-field spatial distributions.

References

1. F. Benz, *et al.*, Single-molecule optomechanics in "picocavities." *Science* **354**, 726–729 (2016).
2. M. Urbieta, *et al.*, Atomic-Scale Lightning Rod Effect in Plasmonic Picocavities: A Classical View to a Quantum Effect. *ACS Nano* **12**, 585–595 (2018).
3. Carnegie, C. et al., Flickering nm-scale disorder in a crystal lattice tracked by plasmonic 'flare' light emission. *under review Nat. Commun.* (2019).
4. B. de Nijs, *et al.*, Unfolding the contents of sub-nm plasmonic gaps using normalising plasmon resonance spectroscopy. *Faraday Discuss.* **178**, 185–193 (2015).
5. R. Chikkaraddy, *et al.*, How Ultranarrow Gap Symmetries Control Plasmonic Nanocavity Modes: From Cubes to Spheres in the Nanoparticle-on-Mirror. *ACS Photonics* **4**, 469–475 (2017).
6. P. Atkins, J. dePaula, *Physical Chemistry: Thermodynamics, structure, and change* (Macmillan Higher Education, 2014).